Synthesis and Characterization of Iron(II) Complexes Modeling the Active Site Structure of Nonheme Iron Dioxygenases

Jacob Baus
Marquette University, jacob.baus@marquette.edu

SYNTHESIS AND CHARACTERIZATION OF IRON(II) COMPLEXES MODELING THE ACTIVE SITE STRUCTURE OF NONHEME IRON DIOXYGENASES

by

Jacob S. Baus

A Thesis submitted to the Faculty of the Graduate School,
Marquette University,
in Partial Fulfillment of the Requirements for
the Degree of Master of Science

Milwaukee, Wisconsin

May 2012

ABSTRACT
SYNTHESIS AND CHARACTERIZATION OF IRON(II) COMPLEXES MODELING THE ACTIVE SITE STRUCTURE OF NONHEME IRON DIOXYGENASES

Jacob S. Baus

Marquette University, 2012

The aerobic degradation of polycyclic aromatic compounds, which are widespread contaminants in soils and groundwaters, is carried-out in large part by various Fe-containing dioxygenases that perform the *cis*-dihydroxylation and oxidative cleavage of aromatic rings. Recently, a new Fe dioxygenase family emerged that catalyzes a remarkable set of transformations; the distinguishing feature of these enzymes is that their monoiron(II) centers are coordinated by three histidines residues (i.e., imidazole ligands) in a facial geometry – a departure from the "canonical" 2-histidine-1-carboxylate facial triad that is dominant among nonheme monoiron enzymes. Members of the "3His family" are capable of oxidatively cleaving C-C bonds in substrates that are generally resistant to degradation, including β-diketones and monohydroxylated aromatics (e.g., salicylic acid). This thesis describes the design, synthesis, and characterization of novel transition-metal complexes with polyimidazole ligands that serve as faithful structural and functional models of these important metalloenzymes. Specifically, high-spin iron(II) β-diketonato complexes were synthesized with the ^{Ph}TIP (tris(2-phenylimidazol-4-yl)phosphine), and ^{tBu}TIP ((tris-2-*tert*-butylimidazol-4-yl)phosphine) ligands. The complexes were analyzed with a combination of experimental and computational methods including X-ray crystallography, cyclic voltammetry, UV-vis absorption, ^{1}H nuclear magnetic resonance, and density functional theory (DFT). The resulting geometric- and electronic-structure descriptions were compared with those obtained for analagous models with the anionic ^{Me2}Tp (hydrotris(3,5-dimethylpyrazol-1-yl)borate) and ^{Ph2}Tp (hydrotris(3,5-diphenylpyrazol-1-yl)borate) ligands. A similar biomimetic approach was employed in the synthesis and characterization of models of the enzyme salicylate 1,2-dioxygenase.

ACKNOWLEDGMENTS

Jacob S. Baus

I would like to thank my parents, Stephen and Evelyn Baus for their love and support. Thanks to Drs. Brant Kedrowski, William Wacholtz, and Jonathon Gutow at the University of Wisconsin ~ Oshkosh for all the direction and knowledge they gave me, Michael Bittner for going through all the trials of graduate school alongside me, and special thanks to Dr. Adam Fiedler for all that he has done for me during my time at Marquette.

TABLE OF CONTENTS

LIST OF TABLES

LIST OF FIGURES

Chapter 1

Structural and Catalytic Properties of Nonheme Fe Dioxygenases Involved in Bioremediation Processes

Abstract: The selective oxidation of hydrocarbons and their derivatives is important in numerous industrial and petrochemical processes. The demanding nature of these transformations often requires the use of toxic and expensive oxidants; however, biological systems have evolved various metalloenzymes that catalyze similar reactions using dioxygen (O_2) as the sole oxidant. For instance, mononuclear nonheme Fe dioxygenases are capable of performing challenging oxidation reactions such as the dihydroxylation of hydrocarbons and oxidative cleavage of C-C bonds. Recently, a new Fe dioxygenase family has emerged that catalyzes a remarkable set of transformations involving organic pollutants; the distinguishing feature of these enzymes is that their Fe(II) centers are coordinated by three histidines (3-His) residues in a facial geometry – a departure from the "canonical" 2-histidine-1-carboxylate triad that is dominant among nonheme monoiron enzymes. While a number of these 3-His dioxygenases have been structurally characterized with X-ray crystallography, uncertainty exists about the mechanism of these enzymes at the molecular level. Our research efforts seek to employ the methods of synthetic inorganic chemistry to address fundamental questions regarding the catalytic activity of nonheme iron dioxygenases with the 3His motif.

1.A. The Role of Nonheme Fe Dioxygenases in Biodegradation

The selective oxidation of hydrocarbon feedstocks to more valuable compounds is a vitally important process in the chemical industry. As such transformations often require expensive and harsh oxidants, there has been considerable interest in generating catalytic systems that employ cheap and environmentally-benign oxidants like dioxygen (O_2). Remarkably, Nature has already achieved this goal with numerous metalloenzymes that utilize O_2 to carry out demanding and selective oxidations of biomolecules at ambient temperatures and pressures.[1-5] Detailed biochemical studies of these enzymatic systems, coupled with attempts by synthetic chemists to mimic their structures and functions, offer the possibility of developing efficient "green" catalysts for industrial use.

An important class of enzymes involved in O_2-activation are mononuclear nonheme Fe dioxygenases that breakdown and assimilate aromatic hydrocarbons in microbes.[6-7] For example, naphthalene dioxygenase (NDO) catalyzes the first step in the degradation of naphthalene via oxidation to the corresponding cis-1,2-diol (Scheme 1.1).[8] Following dehydrogenation, the aromatic ring is oxidatively opened by either an intradiol- or extradiol-cleaving catechol dioxygenase (CatD).[9] The resulting products are further degraded to yield small molecules that feed into the Krebs cycle, thereby allowing the organisms to utilize hydrocarbons as sources of energy.[9] Similarly, aminophenol dioxygenases (APDs) perform the oxidative ring-cleavage of substrates derived from the microbial catabolism of nitroaromatics (Scheme 1.1).[10]

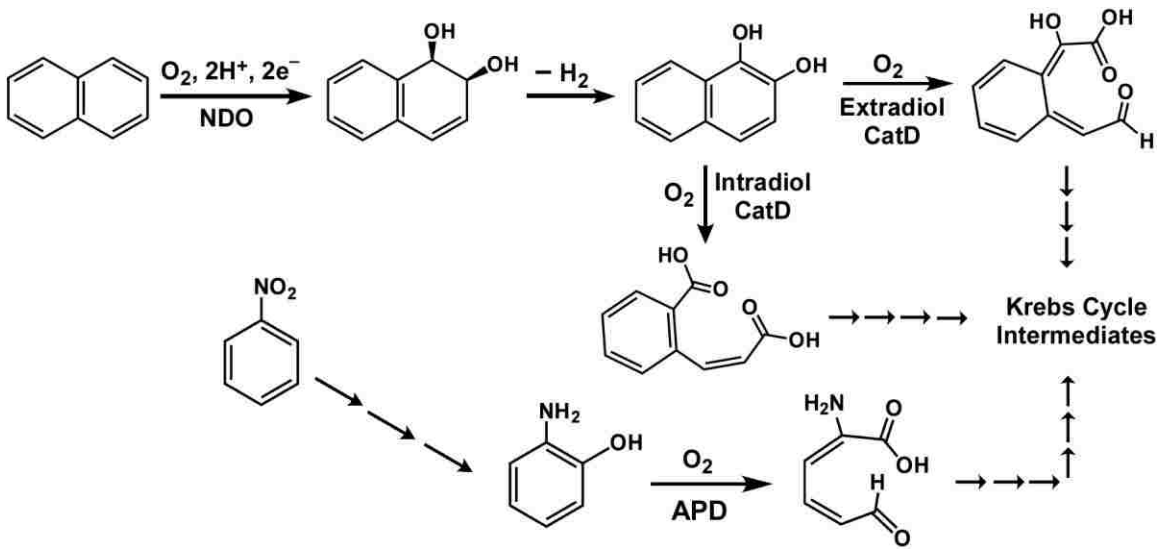

Scheme 1.1.

NDO, extradiol CatDs, and APDs all feature active sites with an Fe^{2+} center coordinated to one aspartate (or glutamate) and two histidine residues in a facial array; two or three bound H_2O molecules are also found in the resting states.[8-9,11-15] This 2-His-1-carboxylate (2H1C) facial triad is the predominant coordination motif among nonheme monoiron enzymes involved in O_2 activation – other examples include the a-ketoglutarate- and pterin-dependent oxygenases and isopenicillin *N*-synthase (IPNS).[16] A key advantage of the 2H1C structural motif is that it permits the Fe center to bind both substrate and O_2 at adjacent coordination sites in an ordered mechanism.

The proposed catalytic cycle for the extradiol CatDs (Scheme 1.2) begins with the coordination of substrate to the Fe center as a bidentate, monoanionic ligand with simultaneous loss of H_2O ligands.[9,17] The resulting five-coordinate Fe^{2+} center is then activated for O_2 binding, perhaps yielding a short-lived ferric-superoxo intermediate.[17] Formation of the Fe/O_2 adduct then triggers one-electron oxidation of the bound substrate and its deprotonation by a nearby His residue, resulting in a putative superoxo-Fe^{2+}-

semiquinonate intermediate. The two Fe-bound radicals then combine to give an Fe(II)-alkylperoxo species that eventually converts to the ring-cleaved product. An intriguing aspect of the proposed mechanism is the tight coupling between dioxygen binding, inner-sphere electron transfer (from Fe to O_2 and substrate to Fe), and proton transfer during formation of the key semiquinonate intermediate.[17] However, it is not clear whether these events occur in a stepwise or concerted manner. Questions also remain concerning the amount of radical character on the substrate ligand in the O_2-bound form of the enzyme.

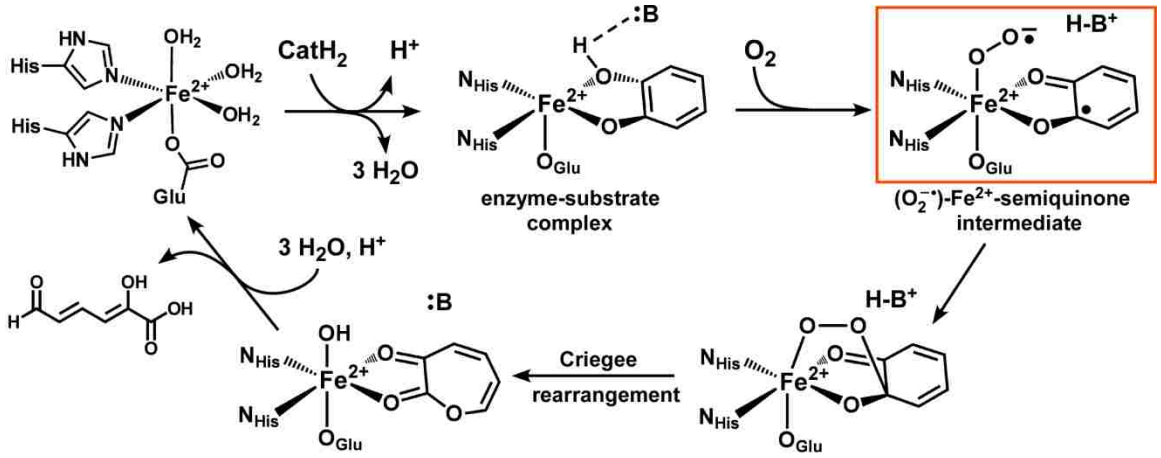

Scheme 1.2.

1.B. A New Class of Nonheme Fe Dioxygenases

Interestingly, a new class of mononuclear nonheme Fe dioxygenases has recently emerged that employ the 3-histidine (3His) facial triad instead of the "canonical" 2H1C facial triad.[18,19] These "3His" enzymes are largely found in bacteria where they act to degrade xenobiotic compounds (an exception is cysteine dioxygenase (CDO), which initiates the catabolism of L-cysteine in mammals;[20,21] (Scheme 1.3). *Members of the "3His family" catalyze novel transformations that have expanded the known boundaries of Fe dioxygenase chemistry.* For example, the enzyme β-diketone dioxygenase (Dke1) converts acetylacetone to acetic acid and 2-oxopropanal (Scheme 1.3) – one of the few Fe-dependent dioxygenases capable of oxidatively cleaving aliphatic C-C bonds. [22,23] X-ray diffraction (XRD) studies confirmed that the metal center in Dke1 is facially coordinated by three His residues and presumably 2-3 H_2O molecules, although these were not resolved in the structure.[24,25] Spectroscopic studies indicate that substrate coordinates to Fe as the deprotonated b-keto-enolate in a bidentate manner.[26] Other newly-discovered Fe dioxygenases with the 3His triad include gentisate 1,2-dioxygenase (GDO)[27] and salicylate 1,2-dioxygenase (SDO).[28-30] Sequence analysis also suggests that 1-hydroxy-2-naphthoate dioxygenase (HNDO) belongs to the 3His family,[30,31] although crystallographic data are currently lacking. Like the CatDs, each of these microbial enzymes participates in hydrocarbon assimilation via the oxidative cleavage of aromatic C-C bonds (Scheme 1.3). Yet SDO and HNDO are unique in performing the oxidation of aromatic rings with only one electron-donating group.

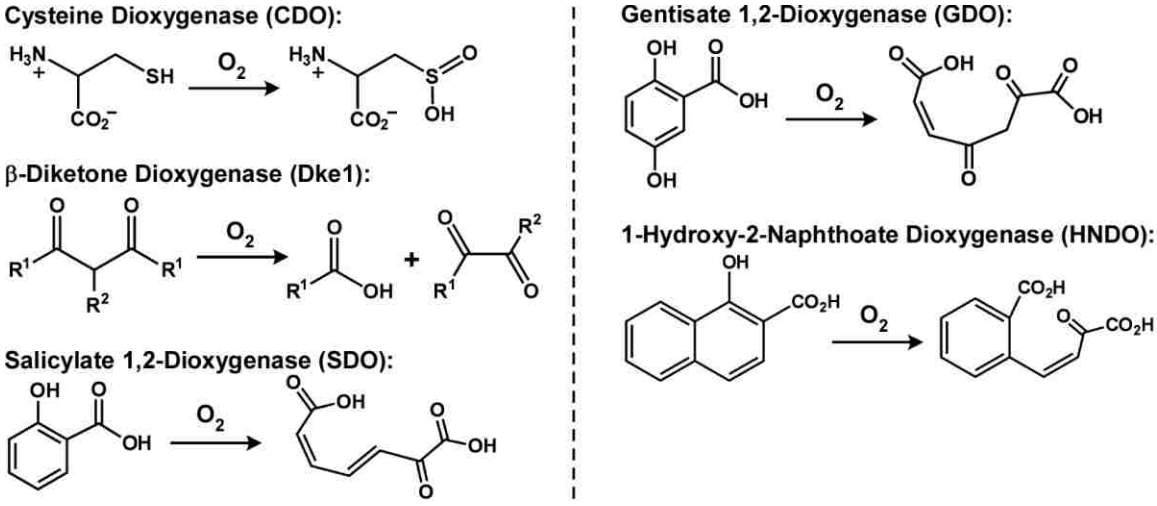

Scheme 1.3.

Dke1 was first isolated from the bacteria *Acinetobacter johnsonii*. Taken from raw sewage, the bacteria was grown in a minimal medium with acetylacetone as its only source of carbon.[22] Acetylacetone is a widely used, toxic industrial chemical, and this bacteria is capable of converting it to acetate and 2-oxopropanal, which is futher degraded into small metabolites that eventually enter the Kreb cycle.[22] Further experiments revealed that acetylacetone is not the only viable substrate,[22,32] since the enzyme is capable of oxidizing a wide range of b-diketones.

X-ray diffraction (XRD) studies confirmed that the metal center in Dke1 is facially coordinated by three His residues and presumably 2-3 H_2O molecules, although these were not resolved in the structure (Figure 1.1).[24,25] While the active site can bind several first-row transition metal ions, only Fe(II) results in catalytic activity.[22] Spectroscopic studies suggest that substrate coordinates to Fe as the deprotonated β-keto-enolate in a bidentate manner.[33]

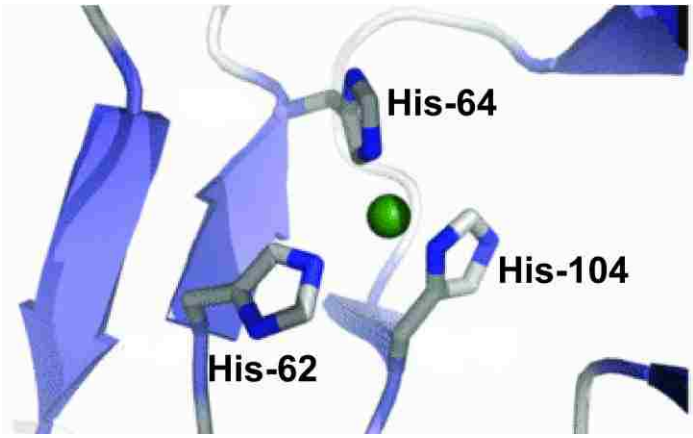

Figure 1.1. Crystal structure of the Dke1 active site.[25]

Given the prevalence and effectiveness of monoiron enzymes with the "canonical" 2H1C triad, the emergence of the 3His family of Fe dioxygenases raises an interesting question: what is the significance of this change in Fe coordination environment for catalysis? Interestingly, a mutant of Dke1 in which the His104 ligand was replaced with Glu was able to partially bind Fe^{2+} (~30% of wild type) yet exhibited no catalytic activity.[25] Similarly, a mutant of IPNS in which the Asp ligand was replaced with His was inactive although it contained approximately the same amount of Fe as the wild type enzyme.[16] Thus, *the 2H1C and 3His motifs are not functionally interchangeable, yet it remains unclear exactly how these ligand-sets tune the catalytic properties of their respective enzymes.*

Another open question concerns the mechanism of oxidative C-C bond cleavage in the 3His dioxygenases. Based on kinetic data for Dke1, Straganz has proposed that the reaction proceeds via direct addition of O_2 to the bound substrate to give an alkylperoxidate intermediate.[33] The nucleophilic peroxidate then attacks the carbonyl group to yield a dioxetane species, which subsequently collapses to the products via concerted C-C and O-O bond cleavage (Scheme 1.4-A). This mechanism resembles the

one proposed for the intradiol CatDs in which the role of the Fe center is to activate substrate, not O_2.[34,35] A more conventional O_2-activation mechanism has also been proposed for Dke1 that involves initial formation of an Fe-superoxo intermediate, followed by reaction with bound substrate (Scheme 1.4-B).[32]

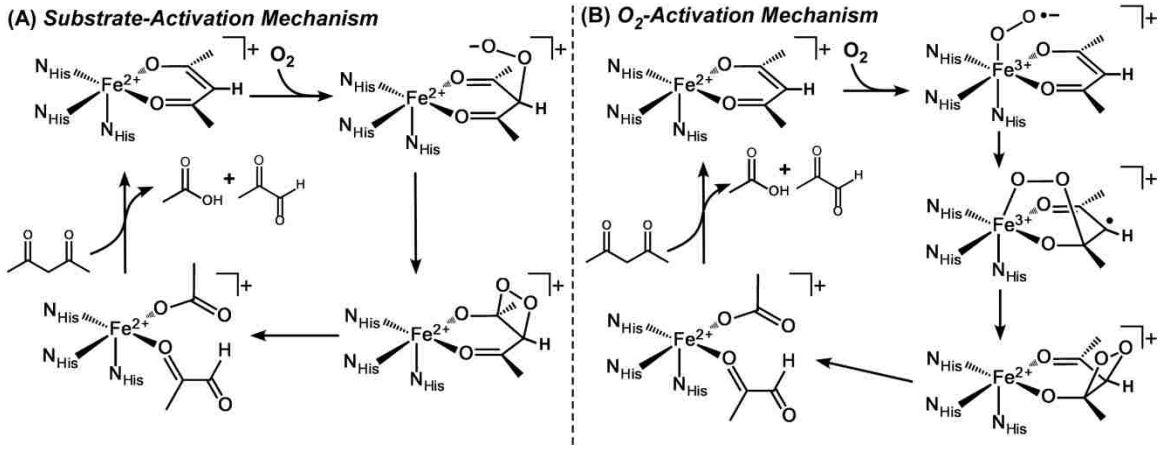

Scheme 1.4.

The mechanisms of SDO and HNDO are also unsettled. The lack of a second electron-donating group on the substrates, noted above, makes it unlikely that these enzymes follow the same catalytic cycle as the extradiol CatDs, which involves a Criegee rearrangement to form a lactone intermediate.[9,36] This step requires ketonization of the second –OH group to transfer electron-density onto the ring – an impossibility for the SDO and HNDO substrates. Thus, these 3His Fe dioxygenases require an alternative strategy for oxidative ring scission that has yet to be determined.

1.C. Value of the Biomimetic Approach

The efficiency and selectivity of metalloenzymes has inspired inorganic chemists to generate synthetic complexes that replicate important structural, spectroscopic, and/or functional properties of the enzyme active sites.[37] Indeed, fruitful interactions between biochemists and synthetic inorganic chemists have greatly advanced our understanding of metalloenzyme function. The unique reactions performed by the 3His family of Fe dioxygenases, as well as their relevance to bioremediation processes, make them worthy targets for biomimetic studies. Thus, the central theme of this research proposal is the design of metal complexes that serve as structural and functional models of dioxygenases with the 3His facial triad (specifically, Dke1 and SDO). A key advantage of this approach is that the properties of our dioxygenase models can be modified in a *straightforward and systematic manner*, allowing us to isolate those factors that play crucial roles in modulating electronic structure and catalytic activity. While similar changes can be made to protein active sites via mutagenesis, such modifications often cause widespread and ill-defined changes in structure that result in loss of activity. For instance, in the 2H1C and 3His families, many variants arising from point mutations of coordinating residues fail to bind Fe(II), and most are catalytically inactive, limiting the information that can be derived from mutagenesis studies.[19,38] In contrast, the flexible synthetic approach described here will provide a series of imidazole-based metal complexes with a broad range of geometric and electronic properties, ligand types, and metal centers. By exploring the reactivities of these various complexes with O_2, we will

be able to formulate *structure-reactivity correlations* that are transferrable to the biological systems.

1.D. Outline of Major Findings

The biomimetic approach described above has been used to address fundamental questions regarding the catalytic activity of dioxygenases with the 3His facial triad. This thesis describes the following major findings:

1. A series of monoiron complexes supported by tris(imidazolyl)phosphine ligands and various bound substrates, including β-diketonates (to mimic Dke1) and salicylate derivatives (to mimic SDO) have been prepared and characterized with X-ray crystallography.
2. The geometric and electronic structures of these complexes have been characterized with a combination of experimental and computational methods; namely, cyclic voltammetry, spectroscopic techniques (UV-vis absorption and electron paramagnetic resonance), and density functional theory (DFT) calculations.

Chapter 2

Synthesis and Characterization of Fe(II) β-Diketonato Complexes with Relevance to Acetylacetone Dioxygenase

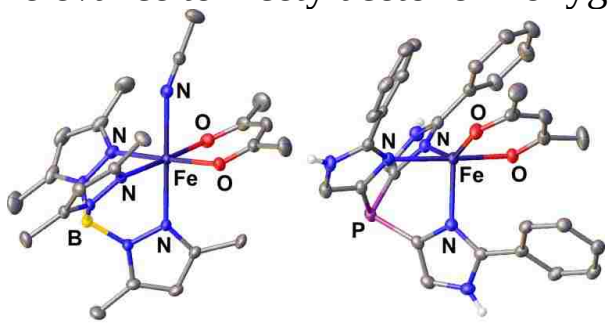

Abstract: A series of high-spin iron(II) β-diketonato complexes have been prepared and characterized with the intent of modeling the substrate-bound form of the enzyme acetylacetone dioxygenase (Dke1). The Dke1 active site features an Fe(II) center coordinated by three histidine residues in a facial geometry – a departure from the standard 2-histidine-1-carboxylate (2H1C) facial triad dominant among nonheme monoiron enzymes. To better understand the implications of subtle changes in coordination environment for the electronic structures of nonheme Fe active sites, synthetic models were prepared with four different supporting ligands (L_{N3}): the anionic ^{Me2}Tp and ^{Ph2}Tp ligands (^{R2}Tp = hydrotris(pyrazol-1-yl)borate substituted with R-groups at the 3- and 5-pyrazole positions) and the neutral ^{Ph}TIP and ^{tBu}TIPligands (^{R}TIP = tris(imidazol-4-yl)phosphine substituted with R-groups at the 2-imidazole position). The resulting $[(L_{N3})Fe(acac^{X})]^{0/+}$ complexes ($acac^{X}$ = substituted β-diketonates) were analyzed with a combination of experimental and computational methods, namely, X-ray crystallography, cyclic voltammetry, spectroscopic techniques (UV-vis absorption and ^{1}H NMR), and density functional theory (DFT).

2.A. Introduction

The aerobic degradation of pollutants relies heavily on mononuclear nonheme iron dioxygenases found in the catabolic pathways of bacteria.[5,6,17] Examples include the Rieske dioxygenases,[8] extradiol catechol dioxygenases,[9,12,39] and (chloro)hydroquinone dioxygenases.[40-42] These enzymes share a common active-site structure in which the Fe(II) center is coordinated to one aspartate (or glutamate) and two histidine residues in a facial array; two or three bound H_2O molecules are also found in the resting states.[13,43] Despite the predominance of the 2H1C motif, a new class of mononuclear nonheme Fe dioxygenases has recently emerged that employ the three histidine (3His) facial triad instead.[18,19] The first member of this class to be structurally characterized was cysteine dioxygenase (CDO), an enzyme that catalyzes the first step in the catabolism of L-cysteine.[20,21] Other 3His enzymes have since been discovered in bacteria, where they act to degrade xenobiotic compounds.[27,28] The enzyme acetylacetone dioxygenase (Dke1), for instance, is one of the few Fe-dependent dioxygenases capable of oxidatively cleaving aliphatic C-C bonds.[22-23,33] Dke1 allows *Acinetobacter johnsonii* to convert the toxic and prevalent pollutant acetylacetone to acetic acid and 2-oxopropanal. X-ray diffraction (XRD) studies confirmed that the metal center in Dke1 is facially coordinated by three His residues and presumably 2-3 H_2O molecules, although these were not resolved in the structure.[24,25] While the active site can bind several first-row transition metal ions, only Fe(II) results in catalytic activity.[22] Spectroscopic and computational studies indicate that substrate coordinates to Fe as the deprotonated β-diketone (acac) in a bidentate manner.[33]

The emergence of the 3His family of Fe dioxygenases raises a pertinent question: what is the significance of variations in Fe coordination environment for the electronic structure and catalytic activity of dioxygneases? Interestingly, a mutant of Dke1 in which the His104 ligand was replaced with Glu was able to partially bind Fe (~30% of wild type) yet exhibited no catalytic activity.[25] Thus, the 2H1C and 3His motifs are not functionally interchangeable, yet it remains unclear exactly how these ligand-sets tune the catalytic properties of their respective enzymes. Another important question concerns the mechanism of oxidative C-C bond cleavage in Dke1. Based on kinetic data, Straganz and coworkers have proposed that the mechanism proceeds via direct addition of O_2 to the bound substrate to give an alkylperoxidate intermediate.[33] Such a mechanism would resemble the one proposed for the intradiol catechol dioxygenases in which the role of the Fe center is to activate the substrate, not O_2.[34,35] Yet others have suggested a more conventional O_2-activation mechanism that involves initial formation of an Fe-superoxo intermediate, followed by reaction with bound substrate.[32]

These fundamental questions concerning the structure and function of Dke1 can be addressed, in part, thorough the development of synthetic model complexes. Two Fe-acac^X complexes related the Dke1 active site have been previously reported. Several years prior to the discovery of Dke1, Kitajima *et al.* published the synthesis and X-ray structure of [(^{iPr2}Tp)Fe(acac)(MeCN)], where ^{iPr2}Tp = hydrotris(3,5-diisopropylpyrazol-1-yl)borate(-1).[44] In 2008, Siewert and Limberg prepared [(^{Me2}Tp)Fe(Phmal)] (Phmal = anion of diethyl phenylmalonate) and demonstrated that reaction with O_2 at room temperature in MeCN resulted in dioxygenolytic ring cleavage of the bound ligand.[32] Thus, both Dke1 models reported to date utilize ^{R2}Tp ligands (Scheme 2.1), which have

been widely employed to replicate the 2H1C facial triad.[43-48] However, these pyrazole-based ligands have limitations as mimics of the 3His facial triad; pyrazole rings have different electronic properties than histidines (*i.e.*, imidazoles) and the overall negative charge of the Tp ligand contrasts with the neutral 3His set of the enzyme. For such reasons, we have also pursued the tris(imidazol-4-yl)phosphine ligands (^{R}TIP, R = Ph or tBu; see Scheme 2.1) to more faithfully replicate the charge and donor strength of the 3His coordination environment.

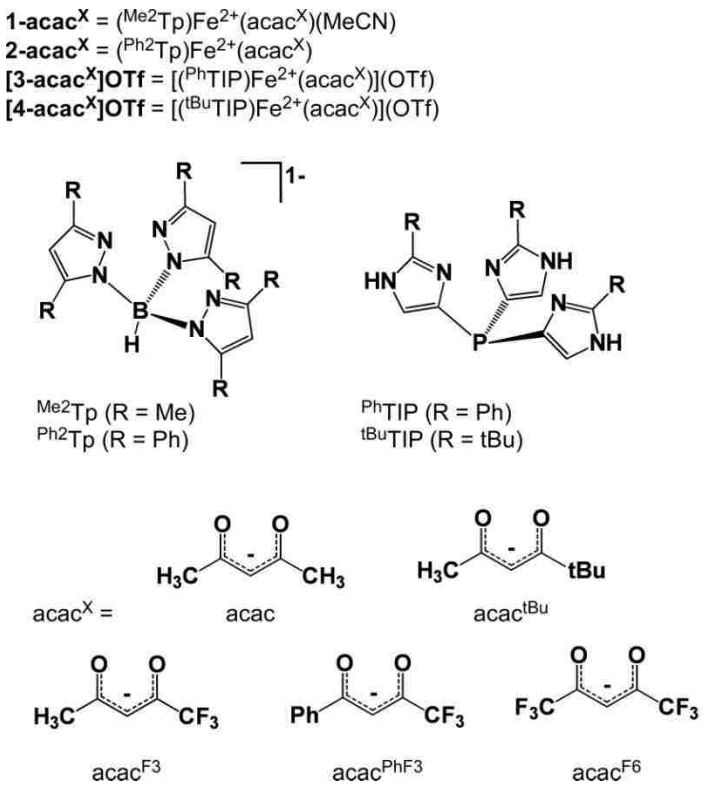

Scheme 2.1.

In an effort to better understand the significance of the 3His triad for Dke1, we have synthesized a series of Fe(II)-acac^{X} complexes featuring the four supporting ligands (L_{N3}) shown in Scheme 2.1: ^{Me2}Tp, ^{Ph2}Tp, ^{Ph}TIP, and ^{tBu}TIP. As noted above, the ^{R2}Tp and ^{R}TIP ligands each reproduce the facial N3 coordination environment of the Dke1

active site, yet they have important differences with respect to charge and electronic properties that resemble those differences between the 2H1C and 3His triads. Since a previous study by Solomon and coworkers suggested that the acac-bound Dke1 site partially retains a bound H_2O ligand,[49] we employed both ^{Me2}Tp and ^{Ph2}Tp ligands in order to generate six-coordinate (6C) and five-coordinate (5C) complexes, respectively. In addition to the natural Dke1 substrate (acac), our models were prepared with acac^X ligands featuring bulky and/or electron-withdrawing substituents (Scheme 2.1) to evaluate the effect such variations on the structural and spectroscopic features of the resulting complexes. Each complex was characterized with X-ray crystallography, cyclic voltammetry, and electronic absorption and ^{1}H NMR spectroscopies. Density functional theory (DFT) calculations were also performed to examine the effects of ligand charge and coordination number on Fe/ligand bonding interactions. This combined experimental and computational approach has provided detailed insights into the electronic structures of the synthetic Fe(II)-acac^X complexes and, by extension, the Dke1 active site.

NOTE: The work involving the Tp-based complexes (**1-acac^X** and **2-acac^X**) was carried out by Dr. Heaweon Park, a postdoctoral researcher in Dr. Fiedler's laboratory. The studies involving the ^{R}TIP-based complexes (**[3-acac^X]OTf** and **[4-acac^X]OTf**) were performed by Jacob Baus.

2.B. Synthesis and Solid State Structures.

Mononuclear Fe(II) β-diketonato complexes with the ^{Ph}TIP and ^{tBu}TIP ligands ([**3-acac^{X}]OTf** and **[4-acac^{X}]OTf**, respectively; Scheme 2.1) were generated via addition of the ligand to MeOH solutions of Na(acac^{X}) and Fe(OTf)$_2$. All syntheses were performed under anaerobic conditions. Each complex was characterized with single-crystal X-ray crystallography, with the exception of **[4-acac^{PhF3}]OTf** and **[4-acac^{F6}]OTf**. Details concerning the XRD data collection and analysis are summarized in the Experimental Section (Table 2.10-11).

Metric data for complexes with the ^{Ph}TIP ligand ([**3-acac^{X}]OTf**; acac^{X} = acac, acac^{F3}, acac^{F6}, and acac^{PhF3}) are provided in Table 2.1, and the crystallographic structures from this series are shown in Figure 2.1. Crystals of these triflate salts were obtained either by the slow cooling of MeCN solutions or diffusion of pentane into CH_2Cl_2 solutions. Analysis of the crystal packing reveals that each triflate counteranion forms hydrogen bonds with three imidazole N-H groups in the solid state. In general, the [**3-acac^{X}]OTf** complexes exhibit 5C Fe(II) geometries that are intermediate between square pyramidal and trigonal bipyramidal (τ-values between 0.38 to 0.56). The lone exception is [**3-acac^{F6}(MeCN)]OTf**, which features a 6C Fe(II) center with a bound solvent ligand (Figure 2.1-D). In the 5C structures, the iron-pyrazole bond lengths (average Fe-N_{Tp} = 2.15 Å) are similar to those observed for other five-coordinate high-spin Fe(II) complexes with Tp ligands,[43,50-53] and the average Fe-O_{acac} bond distances are near 2.02 Å.

The 6C PhTIP-based complex [**3-acac^{F6}(MeCN)]OTf** adopts a distorted octahedral geometry with an MeCN ligand occupying the position *trans* to N5. The Fe-

N/O bonds in this complex (average Fe-N_{imid} = 2.22 Å; average Fe-O_{acac} = 2.09 Å) are significantly longer than those measured for the 5C **3-acac^{X}** complexes due to the increase in coordination number. In the [**3-acac^{F6}(MeCN)]OTf** structure, the presence of the coordinated MeCN ligand forces two Ph rings of the ^{Ph}TIP ligand to adopt orientations perpendicular to the acac^{F6} ligand (Figure 2.1-D). By contrast, in the 5C structures, the Ph rings lie roughly parallel to the plane of the acac^{X} ligand, shielding the vacant coordination site.

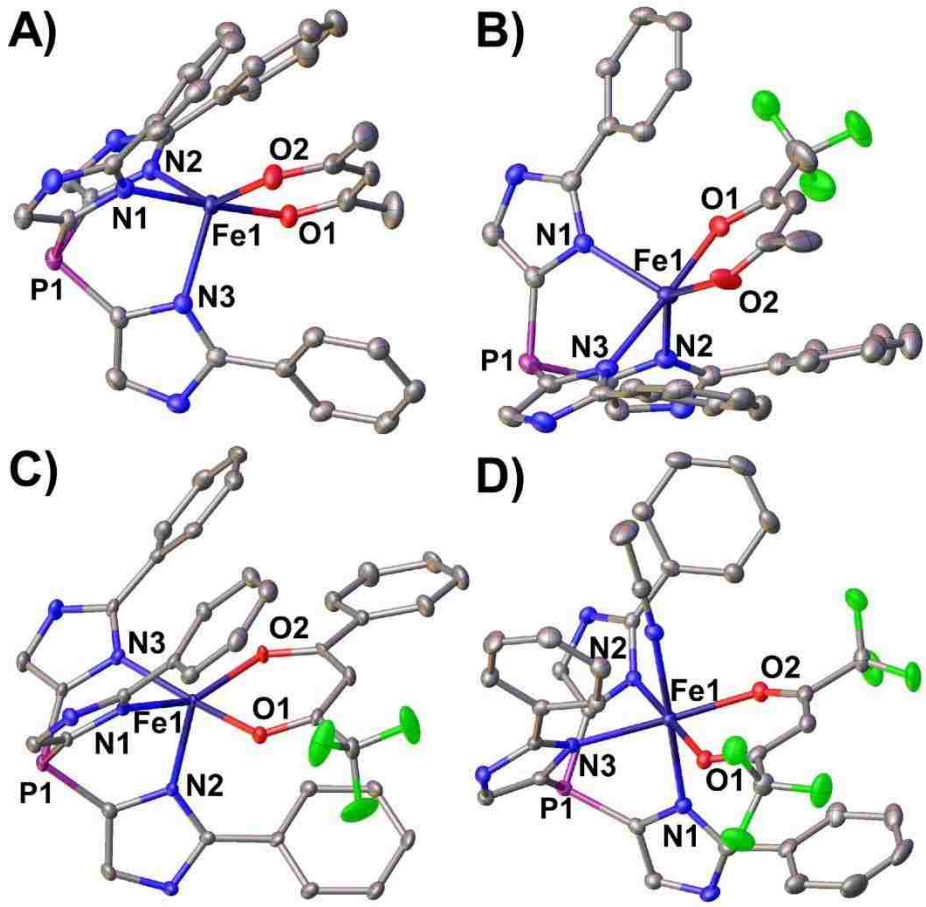

Figure 2.1. Thermal ellipsoid plot (50% probability) derived from A) **[3-acac]OTf**, B) **[3-acac^{F3}]OTf**, C) **[3-acac^{PhF3}]OTf**, and D) **[3-acac^{F6}]OTf**. The counteranions, noncoordinating solvent molecules, and hydrogen atoms have been omitted for clarity.

Table 2.1. Selected bond distances (Å) and angles (deg) for [**3-acac]OTf**•MeCN, **[3-acacF3]OTf**•CH_2Cl_2, [**3-acac^{PhF3}]OTf**•$4CH_2Cl_2$, and [**3-acac^{F6}]OTf**•3MeCN.

Bond Distance	**[3-acac]OTf**•MeCN	[**3-acac^{F3}]OTf**•CH_2Cl_2	[**3-acac^{PhF3}]OTF**•$4CH_2Cl_2$	**[3-acac^{F6}(MeCN)] OTf**•2MeCN
Fe-O1	1.9619(12)	1.930(11)	1.974(2)	2.0792(10)
Fe-O2	2.0586(11)	2.120(11)	2.070(2)	2.0918(11)
Fe-N1	2.2122(13)	2.2225(12)	2.193(3)	2.2639(13)
Fe-N2	2.1212(13)	2.0985(13)	2.109(2)	2.1705(11)
Fe-N3	2.1376(13)	2.1289(12)	2.120(2)	2.2123(13)
Fe-N4				2.1854(14)
Fe-O_{acac}(ave)	2.010	2.025	2.022	2.086
Fe-N_{TIP}(ave)	2.157	2.151	2.141	2.216
Bond Angle				
O1-Fe-O2	87.47(5)	86.5(3)	85.96(9)	83.89(4)
O1-Fe-N1	94.46(5)	96.9(4)	95.77(9)	93.67(4)
O1-Fe-N2	142.76(5)	138.0(8)	150.09(10)	178.87(4)
O1-Fe-N3	123.96(5)	126.7(7)	114.71(9)	89.97(4)
O2-Fe-N1	176.36(5)	176.2(3)	172.64(9)	175.81(5)
O2-Fe-N2	92.12(5)	91.0(3)	89.86(9)	96.03(5)
O2-Fe-N3	90.73(5)	88.5(4)	95.87(9)	92.45(5)
N1-Fe-N2	84.47(5)	85.35(5)	85.08(10)	86.48(5)
N1-Fe-N3	90.75(5)	90.62(5)	89.92(9)	90.95(5)
N2-Fe-N3	93.28(5)	95.04(5)	95.17(9)	88.90(5)
τ-value [a]	0.560	0.637	0.376	–

[a] The geometric parameter τ is defined as $\tau = |(\alpha - \beta)|/60$, where α and β are the two basal angles in pseudo-square pyramidal geometry. The τ-value in 0.0 in idealized square-planar geometries and 1.0 in idealized trigonal bipyramidal geometries.[54]

X-ray quality crystals of the complex [Fe(^{tBu}TIP)(acac)]OTf (**[4-acac]OTf**) were prepared by slow-cooling of a concentrated DCM solution. The ^{tBu}TIP ligand, like ^{Ph}TIP, coordinates in a tridentate, facial manner with an average Fe-N_{imid} distance of 2.19 Å (Table 2.2) – indicative of a high-spin Fe(II) center (S = 2). The acac ligand coordinates in a bidentate fashion with an average Fe-O_{acac} distance of 2.03 Å. A similar coordination geometry was revealed in the X-ray structure of **[4-acac^{F3}]OTf.** In this case, the asymmetric unit included two symmetrically-independent molecules with nearly identical structures (Table 2.2). The ^{tBu}TIP ligand again coordinates in a facial manner

with an average Fe-N_{imid} bond length of 2.16 Å. The acac ligand coordinates in a bidentate fashion with an average Fe-O_{acac} distance of 2.05 Å. For both complexes, the bulky *tert*-butyl substituents of the supporting ligand enforce a trigonal bipyramidal geometry ($\tau \sim 0.74$) with an N_2O equatorial plane.

Comparison of structures with the same coordination number and $acac^X$ ligand indicates that Fe-N bond distances involving the neutral ^{R}TIP ligands are consistently longer than those involving the anionic ^{R2}Tp ligands. For example, the Fe-N_{TIP} bond distances in 6C [**3-acac^{F6}(MeCN)]OTf** are lengthened by ~0.08 Å (on average) relative to the Fe-N_{Tp} distances in **1-acac^{F6}**. Yet this difference is less pronounced when one compares 5C complexes with the same $acac^X$ ligand. In these cases, the Fe-N_{TIP} bond distances are only ~0.02 Å longer (on average) than the corresponding Fe-N_{Tp} bond distances.

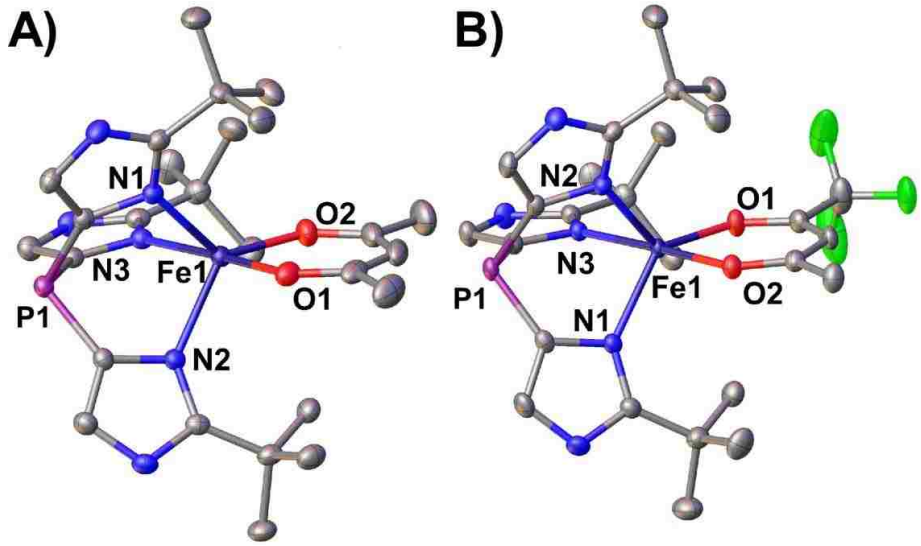

Figure 2.2. Thermal ellipsoid plot (50% probability) derived from A) **[4-acac]OTf**, and B**) [4-acac^{F3}]OTf**. The counteranions, noncoordinating solvent molecules, hydrogen atoms, and the dimer of **[4-acac^{F3}]OTf** have been omitted for clarity.

Table 2.2. Selected bond distances (Å) and angles (deg) for [**4-acac]OTf**•MeCN and **[4-acac^{F3}]OTf**•CH_2Cl_2.

Bond Distance	**[3-acac]OTf**•MeCN	[**3-acac^{F3}]OTf**• CH_2Cl_2
Fe-O1	2.1038(14)	1.988(2)
Fe-O2	1.9642(14)	2.112(2)
Fe-N1	2.1386(15)	2.144(2)
Fe-N2	2.1607(15)	2.137(2)
Fe-N3	2.2564(16)	2.213(2)
Fe-O_{acac}(ave)	2.0340	2.050
Fe-N_{TIP}(ave)	2.1852	2.164
Bond Angle		
O1-Fe-O2	85.45(6)	84.58(9)
O1-Fe-N1	90.51(6)	127.96(10)
O1-Fe-N2	90.97(6)	128.56(10)
O1-Fe-N3	175.41(6)	100.71(9)
O2-Fe-N1	131.44(6)	89.48(9)
O2-Fe-N2	126.78(6)	90.93(9)
O2-Fe-N3	99.11(6)	174.42(9)
N1-Fe-N2	101.62(6)	103.03(9)
N1-Fe-N3	86.08(6)	87.16(9)
N2-Fe-N3	86.71(6)	86.37(9)
τ-value [b]	0.733	0.764

[a] Average values for the two chemically equivalent [**3-acac^{F3}]**$^+$ cations
[b] The geometric parameter τ is defined as τ = |(α - β)|/60, where α and β are the two basal angles in pseudo-square pyramidal geometry. The τ-value in 0.0 in idealized square-planar geometries and 1.0 in idealized trigonal bipyramidal geometries.[54]

2.C. Spectroscopic and Electrochemical Properties

UV-vis absorption spectra of the Fe-acac^{X} complexes, measured in MeCN are shown in Figure 2.3-4. Along with intense near-UV peaks (not shown), two broad absorption manifolds with ε-values between 0.2 and 1.2 $mM^{-1}cm^{-1}$ are observed in the visible region, giving the complexes their distinctive colors. These two features are separated by ~6000-8000 cm^{-1}, although the higher-energy band is often obscured in the **2-acac^{X}** and **[3-acac^{X}]OTf** spectra due to the onset of Ph-based transitions in the near-UV. It is apparent in most spectra that the lower-energy band is comprised of two (or more) overlapping peaks. Within each series, this feature red-shifts as the acac^{X} ligand becomes more electron-poor, suggesting that it primarily arises from an Fe(II)→acac^{X} MLCT transition, an assignment confirmed by literature precedents[49] and time-dependent DFT (TD-DFT) studies. The TD-DFT calculations further indicate that the higher energy feature corresponds to an acac^{X}-based transition with some Fe(II)→acac^{X} MLCT character. The MLCT intensities are strongly dependent on the identity of the acac^{X} ligand, following the order acac^{PhF3} > acac^{F6} > acac^{F3} > acac in each series. A complete summary of absorption energies and intensities are provided in Table 2.3.

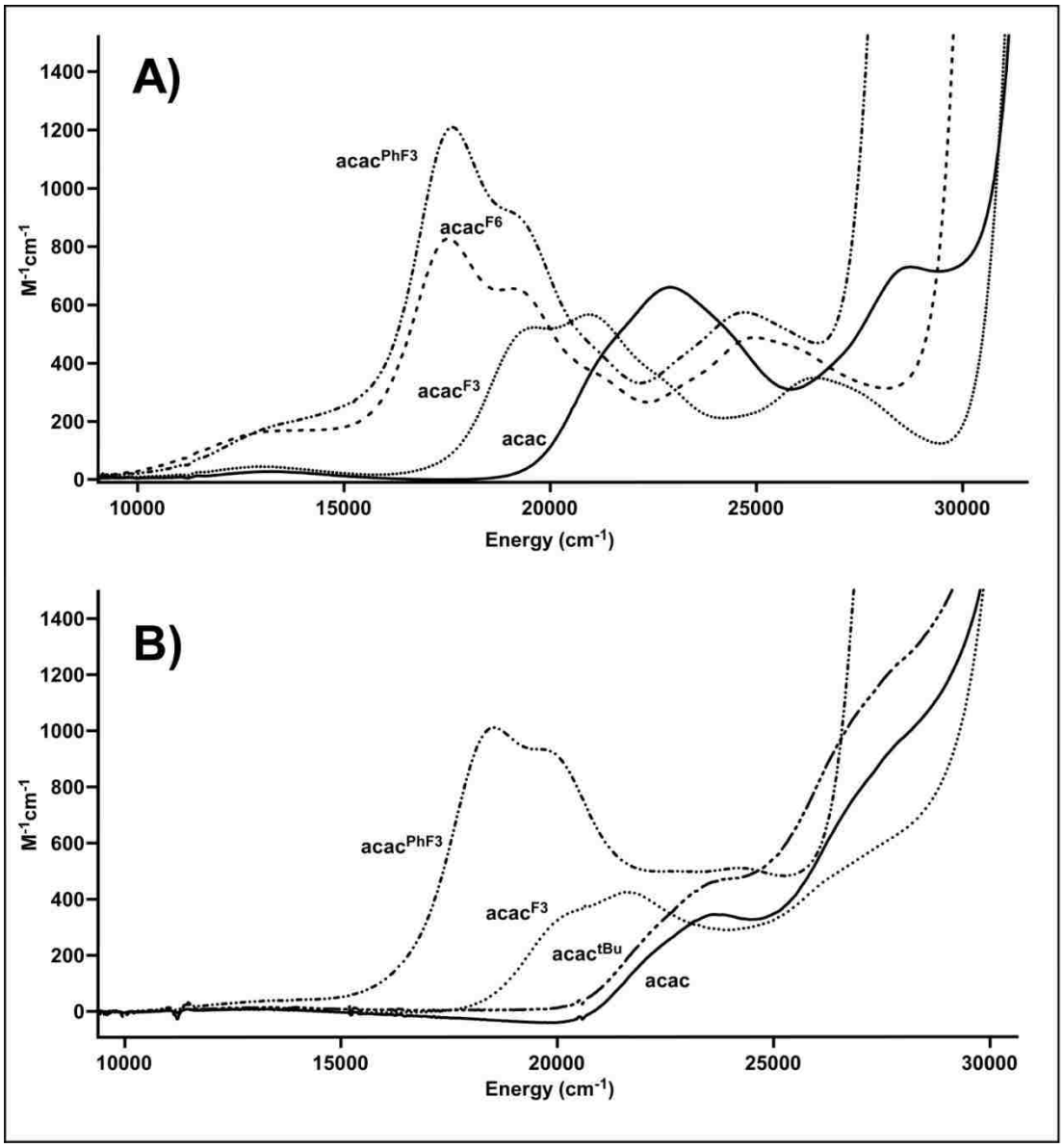

Figure 2.3. Electronic absorption spectra of complexes in the A) **1-acac^{X}** and B) **2-acac^{X}** series measured at room temperature in MeCN.

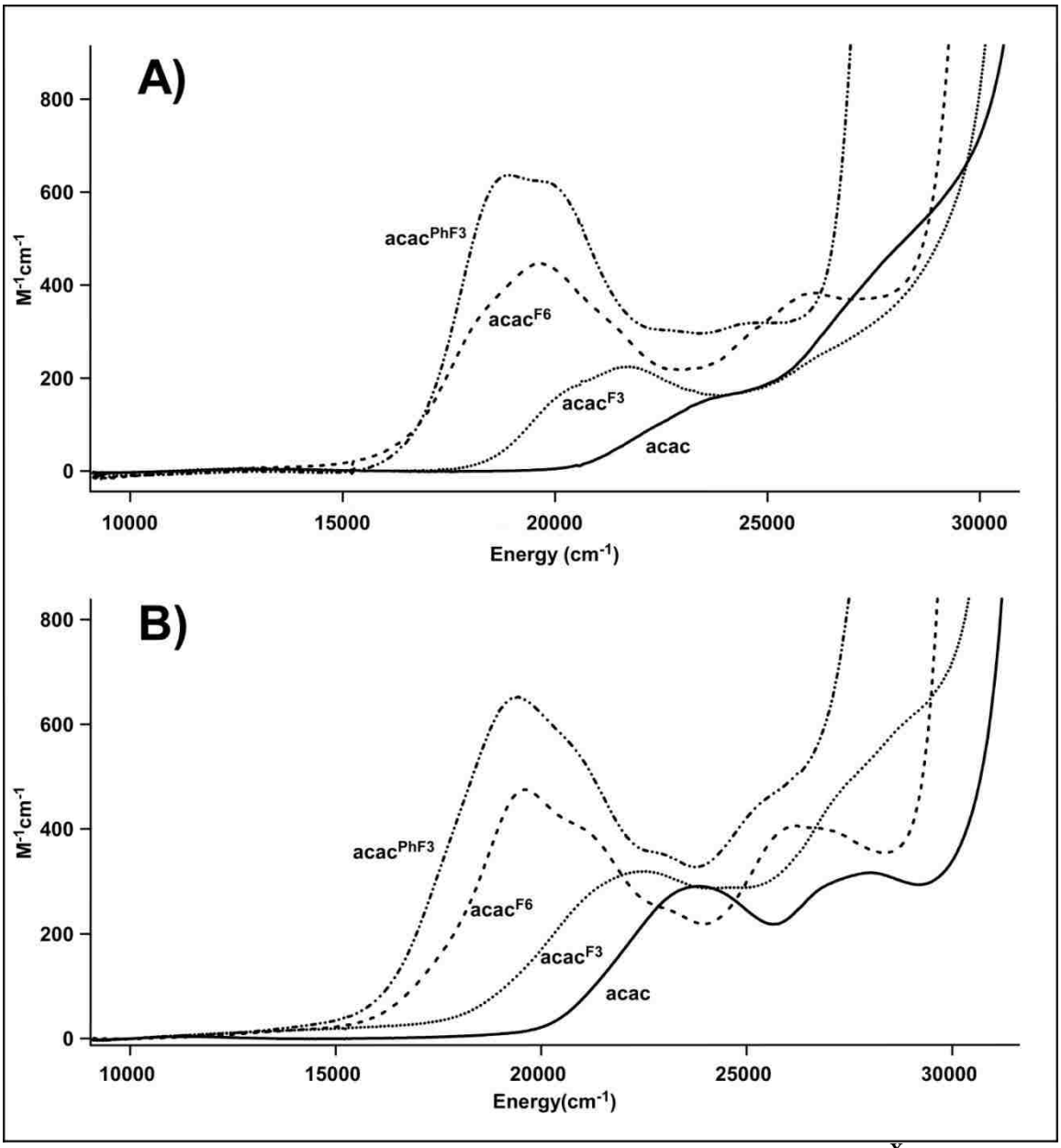

Figure 2.4. Electronic absorption spectra of complexes in the A) [**3-acac^{X}]OTf** and B) **[4-acac^{X}]**OTf series measured at room temperature in MeCN.

It is instructive to compare absorption data for complexes with the same $acac^{X}$ ligand but different supporting ligand. For instance, the MLCT bands of the ^{Ph2}Tp based complexes are blue-shifted by 900 ± 100 cm^{-1} relative to their counterparts in spectra of the ^{Me2}Tp based complexes. Given that these species share virtually identical ligand environments, such significant disparities in absorption energies suggest that the difference in coordination number observed in the solid-state structures persists in solution. The MLCT absorption features of the ^{Ph}TIP complexes are higher in energy than those of the corresponding ^{Me2}Tp and ^{Ph2}Tp complexes by an average of 1400 and 250 cm^{-1}, respectively, where as ^{tBu}TIP complexes are higher by an average of 1650 and 600 cm^{-1}, respectively. This result indicates that the Fe(II) d-orbitals are stabilized in the TIP models relative to the Tp complexes, likely due to the difference in the charge of the supporting ligands. In addition, MLCT absorption features in the TIP series are much weaker than analogous bands in the Tp series (Table 2.3), suggesting that the supporting ligands also modulate the Fe-$acac^{X}$ covalency.

Table 2.3. Physical properties of Fe(II)-acac^{X} complexes and comparison to enzymatic systems.

		UV-vis		Electochemistry
Complex	Color	Energy, cm^{-1}	(ε, $M^{-1}cm^{-1}$)[a]	$E_{1/2}$, mV vs. $Fc^{+/0}$ (ΔE, mV)[b]
1-acac	yellow	22830 (620)	28730 (630)	-303 (72)
1-acac^{F3}	orange	20880 (580)	26520 (400)	-34 (107)
1-acac^{PhF3}	reddish purple	17640 (1190)	24810 (570)	-2 (98)
1-acac^{F6}	purple	17510 (820)	25130 (560)	+225 (127)
2-acac	yellow	23810 (410)	28090 (sh)	-58 (127)
2-acac^{tBu}	yellow	23590 (420)	27700 (sh)	+47 (116)
2-acac^{F3}	orange	21650 (440)	27550 (sh)	+158 (91)
2-acac^{PhF3}	purple	18520 (980)	24100 (460)	+195 (94)
[3-acac]OTf	faint yellow	24090 (160)	28490 (sh)	$E_{p,a}$ = +120[c]
[3-acac^{F3}]OTf	orange	21690 (220)	24510 (320)	$E_{p,a}$ = +360[c]
[3-acac^{PhF3}]OTf	reddish purple	18940 (630)	24510 (320)	$E_{p,a}$ = +410[c]
[3-acac^{F6}]OTf	purple	19650 (450)	26180 (390)	N/A
[4-acac]OTf	faint yellow	23870 (290)	28010 (320)	
[4-acac^{F3}]OTf	orange	19460 (650)	25640 (sh)	
[4-acac^{PhF3}]OTf	reddish purple	19460 (650)	35640 (sh)	
[4-acac^{F6}]OTf	purple	19610 (480)	26250 (410)	
Dke1-acac[d]		24000 (1000)	28000 (sh)	
HPPD-acac[d]		23000 (760)	27500 (sh)	
Dke1-acac^{F3} [e]		22200 (270)	26200 (280)	
Dke1-acac^{PhF3} [e]		18500 (350)		

[a] sh = shoulder; no intensity is reported.
[b] $\Delta E = E_{p,a} - E_{p,c}$.
[c] Only $E_{p,a}$ value is provided due to irreversibility, N/A = no electrochemical event observed.
[d] Data obtained from reference 9, HPPD = hydroxyphenylpyruvate dioxygenase.
[e] Data obtained from reference 20.

^{1}H and ^{19}F NMR spectra of complexes **3-acac^{X}** were measured in MeCN-d_3 at ambient temperature. The wide range of observed chemical shifts confirms that these Fe(II) complexes possess high-spin (S = 2) electronic configurations. Assignments were made on the basis of chemical shifts and peak integrations, T_1-relaxation values, and literature precedents. In all cases, the three imidazole ligands are spectroscopically equivalent in solution. ^{1}H NMR data for complexes **3-acac^{X}** are summarized in Table 2.4. Each complex exhibits a downfield resonance near 65 ppm with a T_1-value of 6 ± 1 ms. This peak gradually disappears upon mixing with MeOH-d_4, indicating that it arises from the exchangeable proton of the imidazole moieties. The other intense downfield signal (found between 35 and 50 ppm) also integrates to three protons, and it is assigned to the 5-imidazole protons. Based on similarities to the NMR spectra of the Fe(^{Ph2}Tp) complexes, the fast-relaxing peak (T_1 ~ 1 ms) in the negative δ-region are attributed to the *ortho* protons of the 2-phenyl substituents. The corresponding *meta* and *para* protons appear near 6.5 and 7.8 ppm, respectively. ^{19}F NMR spectra of the three complexes containing fluorinated β-diketones each display two resonances: a sharp peak at -79.2 ppm from the triflate counteranion, and a fast-relaxing feature (T_1 = 6 ± 3 ms) between -45 and -65 ppm derived from the acac^{X} ligands. The chemical shift measured for the triflate counteranions is identical to that observed for [NBu$_4$]OTf in MeCN-d_3. Interestingly, **3-acac^{F6}** exhibits only only one acac^{F6} derived resonance, indicating that the two -CF$_3$ groups are equivalent in solution because of dynamic averaging.

Regardless of the supporting ligand, peaks arising from methyl substituents of the acac and acac^{F3} ligands exhibit upfield chemical shifts ranging from -12 to -21 ppm, where as the range for the Tp complexes is from -7 to -34 ppm. Interestingly, the T_1-

values of the acac-Me resonances fall into two classes: those measured for **1-acac** and **1-acac^{F3}** are near 10 ms, while those measured for **[3-acac]**OTf and **[3-acac^{F3}]**OTf are considerably shorter (~3 ms) and closer to the value found for **2-acac** in benzene-d_6 (3.3 ms). This result suggests that the acac^X ligands adopt different orientations with respect to the Fe(II) center in the two sets of complexes, and provides further evidence that complexes with bulky Ph-substituents remain pentacoordinate even in MeCN solution. In addition, the T_1-values of **3-acac^{F6}** – the only six coordinate ^{Ph}TIP complex in the solid state – are significantly larger than those measured for the other three ^{Ph}TIP/acac^X species, indicating differences in solution structures.

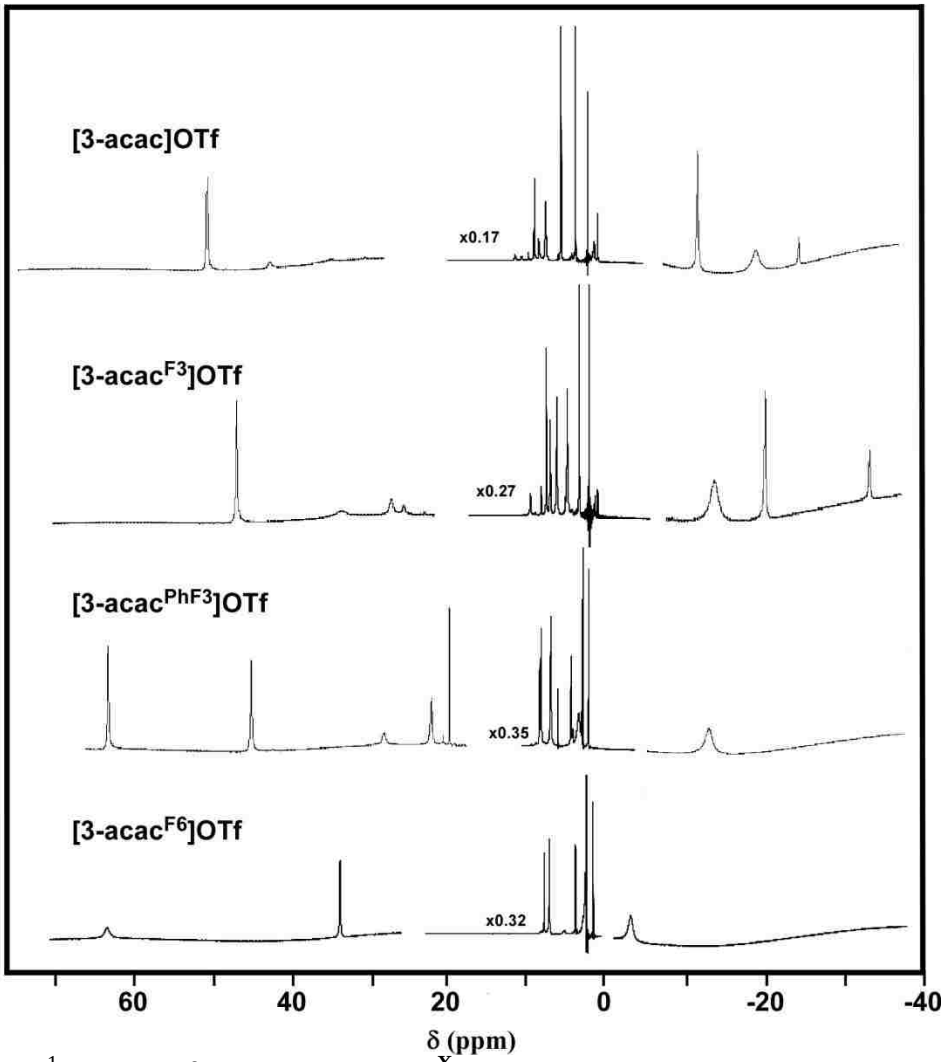

Figure 2.5. ^{1}H NMR of complexes **3-acac^{X}** in MeCN-d_3. Note that peak intensities in the middle portions of the spectra were reduced for the sake of clarity.

Table 2.4. Summary of ^{1}H NMR parameters.

Complex	4-imid δ, ppm	*o*-2-Ph δ, ppm	*m*-2-Ph δ, ppm	*p*-2-Ph δ, ppm	N-H δ, ppm	acac^{X} δ, ppm
[3-acac]OTf	50 (4.0)	-19 (0.45)	6.5 (8.1)	7.8 (23)	65 (5.2)	-12 (-CH_3, 2.9) 44 (-H, 1.0)
[3-acac^{F3}]OTf	47 (4.3)	-14 (0.56)	6.4 (8.9)	7.9 (24)	66 (6.1)	-21 (-CH_3, 3.4) 27.2 (-H, 3.3)
[3-acac^{PhF3}]OTf	45 (4.5)	-13 (0.62)	6.4 (9.3)	7.8 (25)	66 (6.5)	8.0 (*m*-Ph, 35) 16 (*p*-Ph, 77) 19 (*o*-Ph, 2.9)
[3-acac^{F6}]OTf	35 (8.0)	-4.5 (1.2)	7.2 (15)	7.8 (33)	67 (7.0)	5.1 (-H, 3.3)

Spectra for **3-acac^{X}** were taken in MeCN-d_3. The numbers in parenthesis are the relaxation times (T_1) in milliseconds

The redox properties of the Fe-acac^{X} complexes were examined with cyclic voltammetry in MeCN solutions with $(NBu_4)PF_6$ as the supporting electrolyte. The electrochemical data are summarized in Table 2.3 (potentials are reported vs. $Fc^{+/0}$), while Figure 2.6 displays representative cyclic voltammograms for complexes with the acac^{PhF3} ligand. As expected, within each series the redox potentials shift to more positive values as the acac^{X} ligand becomes more electron-poor ($E_{acac} < E_{acacF3} < E_{acacPhF3} < E_{acacF6}$). Potentials measured for the **2-acac^{X}** complexes are 210 ± 25 mV more positive than those in the **1-acac^{X}** series. As shown in Figure 2.6, the ^{Ph}TIP complex **3-acac^{PhF3}** displays an anodic wave at +410 mV along with a much weaker cathodic wave at +190 mV. Such irreversible redox behavior is typical of the **3-acac^{X}** complexes, and thus only the $E_{p,a}$ values are provided in Table 2.3 (**3-acac^{F6}** failed to show any electrochemical events in the range examined). Regardless, the data clearly indicate that the **3-acac^{X}** complexes are harder to oxidize than the corresponding ^{R2}Tp based complexes, with $E_{p,a}$ values shifted positively by 100-200 mV relative to the ^{Ph2}Tp series. Thus, the electrochemical results are consistent with the trend observed for $Fe^{II}\rightarrow acac^{X}$ MLCT energies from DFT calculations; both sets of data indicate the Fe(II) oxidation state is stabilized in the order ^{Ph}TIP > ^{Ph2}Tp > ^{Me2}Tp.

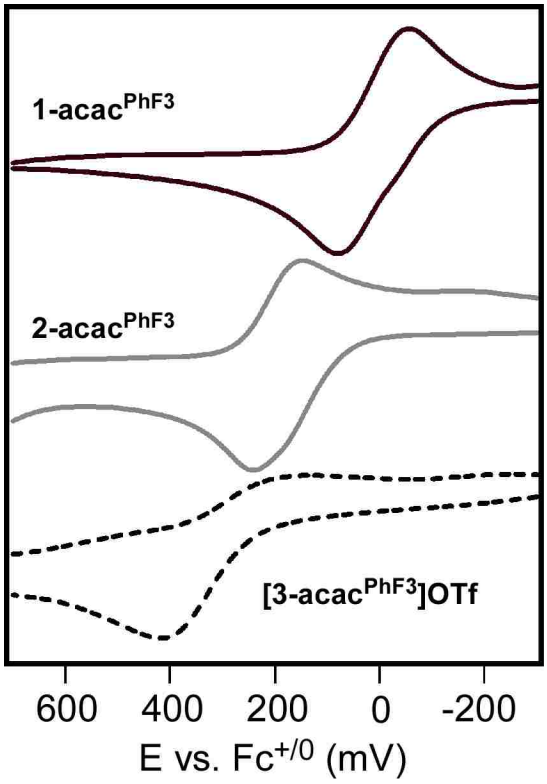

Figure 2.6. Cyclic voltammograms of **1-acac^{PhF3}**, **2-acac^{PhF3}**, and **[3-acac^{PhF3}]OTf** in MeCN (or 1:1 MeCN:CH_2C_{l2} for **2-acac^{PhF3}**) with 60 mM $(NBu_4)PF_6$ as the supporting electrolyte and a scan rate of 100 mV/s.

2.D. O_2 and NO Reactivity

These Fe(II) complexes in the [**3-acac^{X}**]$^{+}$ and [**4-acac^{X}**]$^{+}$ series are generally unreactive towards O_2 in both coordinating and non-coordinating solvents, exhibiting only slow decay at room temperature. It is tempting to ascribe this lack of reactivity to the increased steric bulk of the phenyl substituents, which appear to limit access to the vacant coordination site in the X-ray crystal structures (Figure 2.1-2). However, this hypothesis is contradicted by our experiments with NO.

Each Dke1 model with the ^{Ph}TIP ligand rapidly reacts with NO to yield the corresponding {FeNO}^{7} species (according to the Enemark-Feltham notation). As shown in Figure 2.7, formation of the greenish-brown Fe-NO adduct, [**3-acac(NO)**]$^{+}$, is evident in the appearance of two absorption bands near 440 and 620 nm that are characteristic of 6C {FeNO}^{7} species. While the iron nitrosyl complexes with ^{R2}Tp supporting ligands have long lifetimes at RT, the **3-acac(NO)** species is only moderately stable at -40 ^{o}C in MeCN. The nitrosyl complexes are uniformly high-spin (S = 3/2), displaying nearly axial EPR spectra with $g_x \approx g_y \approx 4.0$ and $g_z = 2.0$ (Figure 2.7, inset).

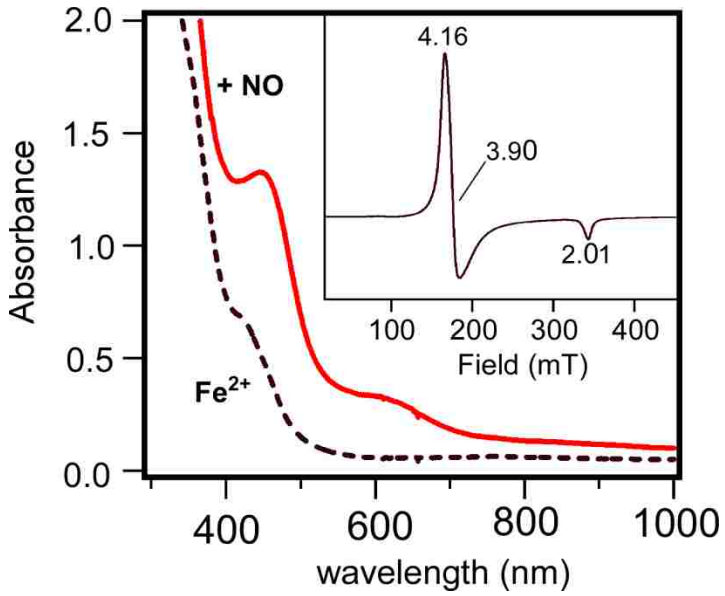

Figure 2.7. Absorption spectra of **3-acac** in MeCN at -40 ^{o}C before and after addition of NO. [Fe] = 2.1 mM. Inset: X-band EPR spectrum of the Fe-NO adduct of **3-acac** in frozen MeCN. Instrumental parameters: frequency = 9.629 GHz; power = 2.0 mW; modulation = 12 G; temperature = 10 K.

2.E. Density Functional Theory (DFT) Calculations.

Energy-minimized structures of the Fe-acac^{X} complexes were generated via DFT geometry optimizations. Based on the crystallographic results, computational models of the **1-acac^{X}** complexes included a bound MeCN ligand, while those of the **2-acac^{X}** series were exclusively 5C. For the sake of comparison, structures of the **[3-acac^{X}]$^{+}$** complexes were computed both with and without coordinated MeCN. The DFT-derived structures agree quite well with the crystallographic results, generally providing bond distances within 0.05 Å of the experimental values. Consistent with the XRD data, DFT predicts Fe-N_{TIP} bond distances to be 0.103 ± 0.002 Å longer (on average) than Fe-N_{Tp} distances for 6C complexes and 0.023 ± 0.002 Å longer for 5C complexes, assuming the same

acac^{X} ligand. However, DFT uniformly overestimates all Fe-$N_{Tp/TIP}$ bond lengths by approximately 0.03 Å, regardless of L_{N3} ligand, while underestimating the Fe-O_{acac} by the same amount. In addition, the computed 5C models tend to exhibit larger τ-values (i.e., geometries closer to the trigonal-bipyramidal limit) than the experimental structures.

Spin-unrestricted single-point DFT calculations utilizing the B3LYP hybrid functional were performed with the optimized models. Representative molecular orbital (MO) energy-level diagrams are shown in Figure 2.8 for **1-acac^{F6}** and **[3-acac^{F6}(MeCN)]$^{+}$**. The lone spin-down Fe electron lies in the $3d_{xz}$-based MO that bisects the N_{eq}-Fe-O angles, while the highest-occupied acac-based MO exhibits a large lobe of electron density on the central carbon atom that reflects the anionic nature of the ligand (Figure 2.9). The spin-down LUMO has mainly acac^{F6} C=O* character, albeit with non-negligible Fe character (~7%). The Fe $3d_{xy}$- and $3d_{yz}$-based MOs lie at slightly-higher energies. Thus, the acac LUMO orbital is approximately isoenergetic with the Fe(II) "t_{2g}-set" of orbitals, resulting in significant π-backbonding interactions. Similar bonding patterns were found for all 6C complexes in the **1-acac^{X}** and **[3-acac^{X}(MeCN)]$^{+}$** series, although the strength of the π-backbonding interactions varied according to the electronic properties of the acac^{X} substituents.

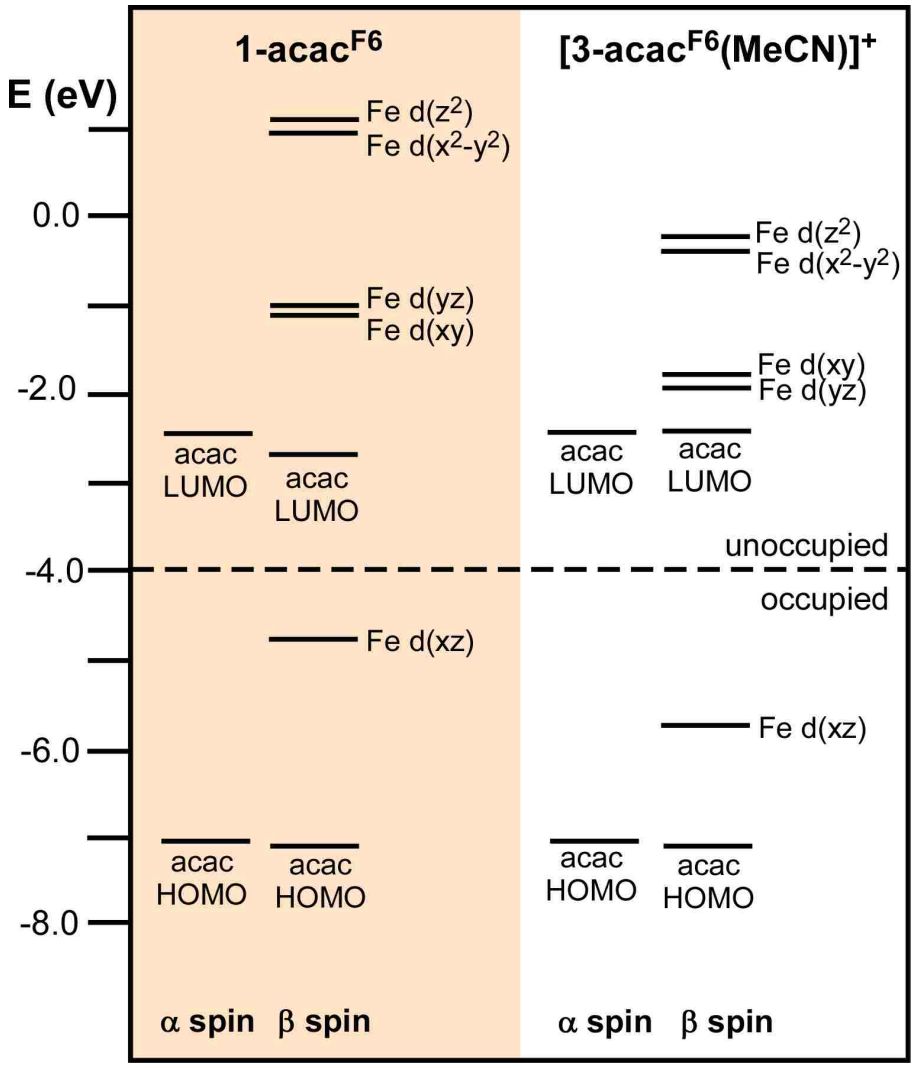

Figure 2.8. MO energy diagrams for geometry-optimized models of **1-acac^{F6}** and **[3-acac^{F6}(MeCN)]$^{+}$** obtained from DFT calculations. To account for differences in overall charge, the computed MO energies for **[3-acac^{F6}(MeCN)]$^{+}$** were uniformly increased by 2.11 eV, such that the acac HOMOs are isoenergetic for the two models (see text for more details).

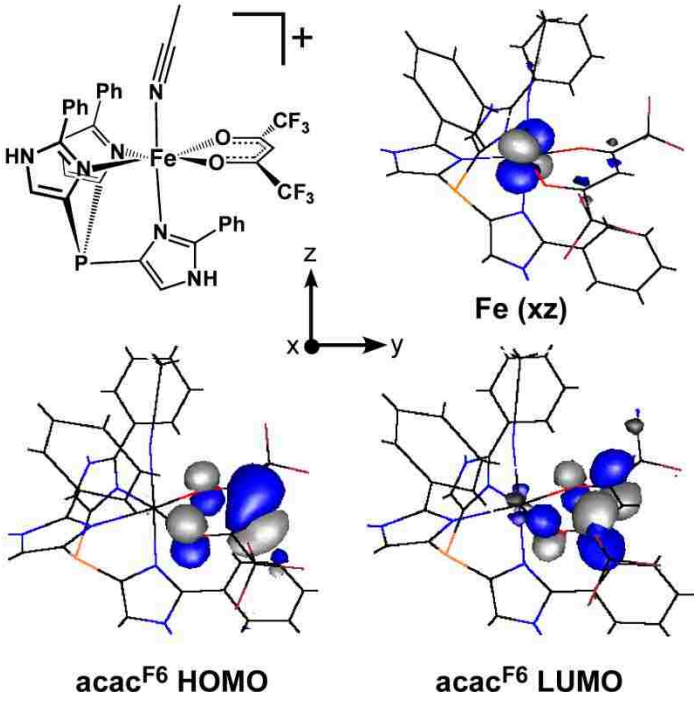

Figure 2.9. Isosurface plots of spin-down MOs computed for **[3-acac^{F6} (MeCN)]$^{+}$** by DFT.

The DFT results permitted further comparison of the electronic properties of the ^{R2}Tp and ^{Ph}TIP supporting ligands. Due to the difference in charge between the two sets of complexes, it was first necessary to normalize the orbital energies. This was accomplished by assuming that the acac HOMO, which is essentially nonbonding with respect to the Fe(II) center and L_{N3} ligand, has identical energies in complexes with the same acac^{X} ligand (that is, the acac^{X} HOMO served as an "internal energy standard"). Following this procedure, it is evident in Figure 2.8 that the Fe d-orbital manifold of **[3-acac^{F6}(MeCN)]$^{+}$** is uniformly stabilized relative to the corresponding set of **1-acac^{F6}** orbitals, reflecting the reduced donor strength of the neutral ^{Ph}TIP ligand compared to the anionic ^{Me2}Tp ligand. Indeed, an analysis of DFT results for the four pairs of 6C Fe-acac^{X} species reveals that Fe d-based MOs in ^{Ph}TIP complexes are stabilized by an

average of 0.9 ± 0.3 eV relative to their counterparts in ^{Me2}Tp models. The contrast between the Tp and TIP ligands is less dramatic for the 5C complexes, where the difference in Fe d-orbital energies is only ~0.3 eV (Figure 2.10 provides MO energy-level diagrams for 5C models of **2-acac^{F3}** and **[3-acac^{F3}]$^{+}$**).

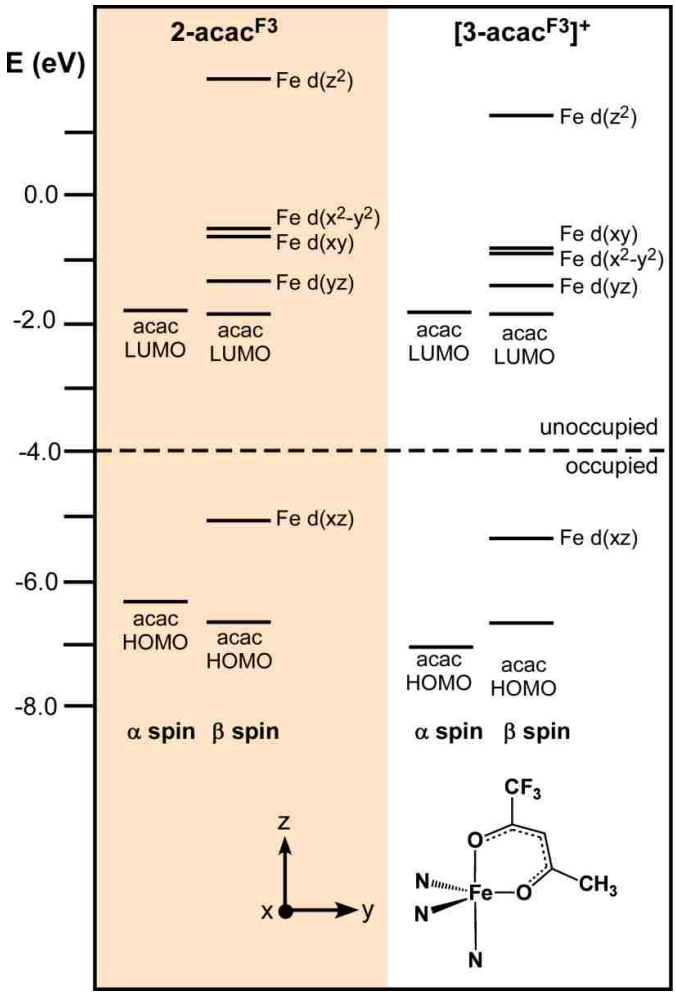

Figure 2.10. MO energy diagrams for geometry-optimized models of **2-acac^{F3}** and **[3-acac^{F3}]$^{+}$** obtained from DFT calculations. To account for differences in overall charge, the computed MO energies for **[3-acac^{F3}]$^{+}$** were uniformly increased by 2.41 eV, such that the acac HOMOs are isoenergetic for the two models (see main text for more details).

To aid in assignment of the observed UV-vis absorption features, time-dependent DFT (TD-DFT) calculations were performed for both 5C and 6C models of the **[3-acac^{X}]$^{+}$** complexes. Regardless of coordination number, TD-DFT predicts two intense features in the visible region: a Fe(xz) → acac^{X} MLCT transition and a higher-energy acac^{X}-based transition with some MLCT character. As shown in Table 2.5, the computed energies for both types of transitions agree reasonably well with the experimental data. While TD-DFT consistently overestimates the MLCT intensities, it nicely reproduces the trend (observed experimentally) that these transitions weaken as the acac^{X} ligand becomes more electron rich. The MLCT transitions are most intense for the 6C complexes, since overlap between the donor Fe(xz) orbital and the acceptor acac^{X} LUMO is maximized when the acac^{X} ligand lies in the equatorial plane. As the geometry shifts towards trigonal bipyramidal in the 5C complexes, this orbital overlap is reduced. In addition, intermediate τ-values facilitate mixing between the MLCT and acac^{X}-based transitions, thereby increasing the intensity of the latter at the expense of the former in 5C complexes.

Table 2.5. Comparison of Experimental and TD-DFT Computed Transition Energies.

		MLCT		acac^{X}-based	
		E, cm^{-1}	ε, M^{-1}cm^{-1}	E, cm^{-1}	ε, M^{-1}cm^{-1}
[3-acac]$^{+}$	6C DFT	25363	900	25464	70
	5C DFT	26130	600	26130	140
	exp	24090	160	28490	N/A
[3-acac^{F3}]$^{+}$	6C DFT	22597	1500	23683	24
	5C DFT	23542	390	25842	105
	exp	21690	220	26810	N/A
[3-acac^{PhF3}]$^{+}$	6C DFT	20036	2660	22139	270
	5C DFT	20244	1020	22873	830
	exp	18940	630	24510	320
[3-acac^{F6}]$^{+}$	6C DFT	19834	2020	22093	10
	5C DFT			23045	
	exp	19650	450	26180	390

Table 2.6. Comparison of Experimental (XRD) and DFT-Computed **1-acac^{X}** Structures. Bond distances in Å, bond angles in degrees.

	1-acac			1-acac^{F3}			1-acac^{PhF3}			1acac^{F6}		
	XRD	DFT	Δ	XRD	DFT	Δ	XRD	DFT	Δ	XRD	DFT	Δ
Bond Length												
Fe-N1	2.154	2.208	0.054	2.180	2.191	0.011	2.144	2.187	0.044	2.150	2.171	0.021
Fe-N2	2.185	2.211	0.026	2.135	2.182	0.047	2.163	2.191	0.028	2.115	2.170	0.054
Fe-N3	2.175	2.212	0.037	2.214	2.196	-0.018	2.169	2.191	0.022	2.146	2.185	0.039
Fe-O1	2.088	2.046	-0.042	2.056	2.058	0.002	2.074	2.034	-0.040	2.112	2.057	-0.055
Fe-O2	2.051	2.051	0.000	2.084	2.048	-0.037	2.065	2.041	-0.024	2.098	2.054	-0.044
Fe-N_{MeCN}	2.236	2.223	-0.013	2.221	2.248	0.027	2.255	2.252	-0.003	2.246	2.253	0.007
Fe-N_{Tp}(ave)	2.171	2.210	0.039	2.176	2.190	0.013	2.158	2.190	0.031	2.137	2.175	0.038
Fe-O_{acac}(ave)	2.070	2.049	-0.021	2.071	2.053	-0.018	2.070	2.038	-0.032	2.105	2.056	-0.050
Bond Angle												
N1-Fe-N2	85.0	86.1	1.1	87.9	86.4	-1.5	88.5	86.0	-2.5	89.0	86.7	-2.3
N1-Fe-N3	85.4	84.5	-0.9	85.9	85.1	-0.8	86.1	86.5	0.4	88.2	86.5	-1.7
N2-Fe-N3	86.2	85.0	-1.2	84.0	86.5	2.5	85.3	85.3	0.0	85.6	86.6	1.0
O1-Fe-N1	96.7	94.3	-2.4	90.6	94.3	3.7	92.8	93.2	0.4	91.6	93.7	2.1
O1-Fe-N2	178.0	178.0	0.0	177.9	176.3	-1.6	177.8	177.7	-0.1	179.2	176.5	-2.7
O1-Fe-N3	95.0	97.1	2.1	94.4	97.2	2.8	93.0	96.9	3.9	93.9	96.9	3.0
O2-Fe-N1	177.3	177.0	-0.3	174.7	177.8	3.1	175.5	176.0	0.5	173.8	177.0	3.2
O2-Fe-N2	92.4	93.3	0.9	96.7	93.2	-3.5	93.6	94.3	0.7	96.0	93.6	-2.4
O2-Fe-N3	95.1	98.4	3.3	97.6	97.1	-0.5	98.1	97.5	-0.6	95.9	96.5	0.6
O1-Fe-O2	85.9	86.2	0.3	84.8	86.0	1.2	85.2	86.3	1.1	83.5	85.9	2.4
Fe-N-C(CH_3)	159.3	171.0	11.7	161.2	161.1	0.0	171.5	161.0	10.5	169.2	162.5	6.7

Table 2.7. Comparison of Experimental (XRD) and DFT-Computed **2-acac^{X}** Structures. Bond distances in Å, bond angles in degrees.

	2-acac			2-acac^{tBu}			1-acac^{F3}			1acac^{PhF3}		
	XRD	DFT	Δ	XRD	DFT	Δ	XRD	DFT	Δ	XRD	DFT	Δ
Bond Length												
Fe-N1	2.163	2.286	0.123	2.095	2.116	0.021	2.096	2.106	0.010	2.092	2.103	0.011
Fe-N2	2.146	2.116	-0.030	2.260	2.286	0.026	2.178	2.272	0.095	2.231	2.288	0.056
Fe-N3	2.098	2.109	0.010	2.107	2.111	0.004	2.117	2.105	-0.013	2.095	2.107	0.013
Fe-O1	1.995	1.956	-0.039	2.049	2.029	-0.020	2.050	2.029	-0.021	2.054	2.012	-0.042
Fe-O2	2.024	2.022	-0.001	1.944	1.951	0.007	1.986	1.959	-0.027	1.967	1.962	-0.004
Fe-N_{Tp}(ave)	2.136	2.170	0.034	2.154	2.171	0.017	2.130	2.161	0.031	2.139	2.166	0.027
Fe-O_{acac}(ave)	2.009	1.989	-0.020	1.997	1.990	-0.006	2.018	1.994	-0.024	2.010	1.987	-0.023
Bond Angle												
N1-Fe-N2	81.7	81.4	-0.3	82.9	81.3	-1.6	83.1	81.6	-1.5	84.7	81.6	-3.1
N1-Fe-N3	91.3	86.1	-5.2	92.7	95.6	2.9	91.2	95.2	4.0	92.2	95.6	3.4
N2-Fe-N3	89.9	94.6	4.7	86.2	85.4	-0.8	89.8	86.0	-3.8	86.9	85.0	-1.9
O1-Fe-N1	91.2	91.0	-0.2	94.6	97.7	3.1	94.8	97.7	2.9	95.9	96.2	0.3
O1-Fe-N2	158.7	138.7	-20.0	177.4	179.0	1.6	172.6	178.6	6.0	177.7	177.2	-0.5
O1-Fe-N3	110.4	125.4	15.0	94.6	95.1	0.5	97.3	95.3	-2.0	95.3	93.5	-1.8
O2-Fe-N1	164.3	178.3	14.0	140.9	137.3	-3.6	152.9	139.0	-14.0	144.5	137.4	-7.0
O2-Fe-N2	92.6	97.7	5.0	93.4	92.1	-1.3	92.3	91.3	-1.0	91.0	94.3	3.3
O2-Fe-N3	103.4	95.5	-7.9	126.0	126.1	0.1	115.5	124.7	9.2	122.8	126.4	3.5
O1-Fe-O2	88.8	88.7	-0.1	88.1	88.4	0.3	86.4	88.4	2.0	87.2	88.5	1.3
τ-value	0.09	0.66	0.57	0.61	0.70	0.09	0.33	0.66	0.33	0.56	0.66	0.11

Table 2.8. Comparison of Experimental (XRD) and DFT-Computed **3-acac^{X}** Structures. Bond distances in Å, bond angles in degrees.

	2-acac				2-acac^{tBu}				1-acac^{F3}				1acac^{PhF3}		
Coord. Number	5	5	5	6	5	5	5	6	5	5	5	6	6	6	6
	XRD	DFT	Δ	DFT	XRD	DFT	Δ	DFT	XRD	DFT	Δ	DFT	XRD	DFT	Δ
Bond Length															
Fe-N1	2.212	2.317	0.105	2.363	2.223	2.314	0.091	2.331	2.193	2.300	0.107	2.288	2.263	2.292	0.029
Fe-N2	2.121	2.130	0.009	2.305	2.098	2.119	0.021	2.279	2.109	2.132	0.023	2.311	2.170	2.262	0.092
Fe-N3	2.138	2.132	-0.006	2.279	2.129	2.124	-0.005	2.275	2.120	2.129	0.009	2.273	2.212	2.275	0.063
Fe-O1	1.962	1.948	-0.013	2.032	1.930	1.957	0.027	2.047	1.974	1.949	-0.025	2.029	2.080	2.052	-0.028
Fe-O2	2.059	2.019	-0.039	2.022	2.120	2.030	-0.090	2.027	2.070	2.020	-0.050	2.030	2.093	2.039	-0.054
Fe-N_{MeCN}				2.163				2.167				2.178	2.184	2.171	-0.013
Fe-N_{TIP}(ave)	2.158	2.193	0.035	2.316	2.150	2.186	0.036	2.295	2.141	2.187	0.046	2.291	2.215	2.276	0.061
Fe-O_{acac}(ave)	2.010	1.984	-0.026	2.027	2.026	1.993	-0.032	2.037	2.022	1.985	-0.037	2.030	2.087	2.046	-0.041
Bond Angle															
N1-Fe-N2	84.5	87.3	2.9	84.5	85.4	84.5	-0.9	84.9	85.1	83.2	-1.9	85.1	86.5	85.3	-1.2
N1-Fe-N3	93.3	83.7	-7.0	90.0	90.6	85.8	-4.8	90.3	89.9	87.6	-2.3	86.0	91.0	91.9	0.9
N2-Fe-N3	90.7	98.7	5.4	86.3	95.0	100.4	5.4	87.3	95.2	99.5	4.3	91.6	88.9	86.6	-2.3
O1-Fe-N1	94.5	91.5	-3.0	91.0	96.9	95.0	-1.9	91.5	95.8	95.0	-0.8	99.0	93.6	90.0	-3.6
O1-Fe-N2	142.8	124.5	-18.3	173.4	138.0	132.5	-5.5	175.1	150.1	140.0	-10.1	170.9	178.9	173.5	-5.4
O1-Fe-N3	124.0	136.3	12.3	88.9	126.7	127.0	0.3	89.4	114.7	120.4	-5.7	96.8	89.9	88.3	-1.6
O2-Fe-N1	176.4	177.8	1.5	172.6	176.2	176.4	0.2	174.2	172.6	174.4	1.8	172.6	175.8	172.0	-3.8
O2-Fe-N2	92.1	94.2	2.1	98.5	91.0	93.2	2.2	97.6	89.9	91.5	1.6	90.4	96.0	98.4	2.4
O2-Fe-N3	90.7	94.6	3.9	96.9	88.5	92.0	3.5	95.1	95.9	93.5	-2.4	88.2	92.4	95.3	2.9
O1-Fe-O2	87.5	88.9	-8.6	86.6	86.5	88.5	-1.0	86.4	86.0	88.0	2.0	86.3	83.9	86.0	2.1
Fe-N-C(CH_3)				171.1				170.5				167.2	174.9	169.4	-5.5
τ-value	0.56	0.89	0.33		0.64	0.73	0.09		0.38	0.57	0.19				

2.F. Summary and Implications for Dke1

This paper has described the synthesis of three series of Fe(II) β-diketonato complexes designed to model the acac-bound form of Dke1 and replicate variations in the facial triad (2H1C vs. 3His) found in nonheme Fe dioxygenases. Adjustment of the steric properties of the Tp ligands resulted in the formation of both 5C and 6C complexes, and β-diketonato ligands with a range of steric and electronic properties were employed to aid in the interpretation of results. Each complex was extensively characterized with experimental and computational methods, including X-ray crystallography, UV-vis and NMR spectroscopies, CV, and DFT calculations. Thus, the sixteen reported complexes have permitted a *systematic examination* of the roles of the L_{N3} and $acac^{X}$ ligands in determining the structural, spectroscopic, electrochemical, and electronic properties of the Fe(II) models. Comparison of complexes featuring anionic (^{R2}Tp) and neutral (^{R}TIP) supporting ligands – but identical $acac^{X}$ ligands – reveals the following key differences: (i) regardless of coordination number, Fe-N_{TIP} bond distances are consistently longer than Fe-N_{Tp} distances (Tables 2.2-3, 2.11-12), (ii) the Fe(II)→$acac^{X}$ MLCT features appear at higher energies for the ^{R}TIP complexes (Figure 2.3-4; Table 2.3), and (iii) redox potentials of the ^{R2}Tp complexes are more negative than those of the corresponding ^{Ph}TIP complexes (Figure 2.6; Table 2.3). DFT calculations further confirm that the ^{Ph}TIP ligand is a significantly weaker donor, as seen in the relative stabilization of the Fe d-orbitals (Figure 2.8). We will now discuss the relevance of these findings for the electronic structure of the Dke1 active site.

Diebold *et al.* recently published a study in which the spectroscopic features of acac-bound Dke1 were compared with those of acac-bound hydroxyphenylpyruvate dioxygenase (HPPD) – an enzyme that possesses the conventional 2H1C facial triad.[27] Prior to that, Straganz and Nidetzky reported the absorption spectra of Dke1 coordinated to various β-diketonates.[33] Like our models, substrate-bound Dke1 exhibits an intense near-UV band and two broad features in the visible region with ε-values between 0.2 and 1.0 $mM^{-1}cm^{-1}$ (Table 2.3). Diebold *et al.* also used CD and MCD spectroscopies to observe much weaker ligand-field transitions at lower energies. Analysis of these ligand-field bands revealed only minor differences between enzymes with the 3His and 2H1C triads; however, the MLCT feature is shifted to lower energy by ~1000 cm^{-1} in the 2H1C system. Similarly, for our synthetic $[(L_{N3})Fe^{2+}(acac^{X})]^{0/+}$ complexes, the absorption features of the **1-acac^{X}** series are red-shifted by an average of 1400 cm^{-1} relative to the **[3-acac^{X}]OTf** series. In general, the 5C **2-acac^{X}**, **[3-acac^{X}]OTf**, and **[4-acac^{X}]OTf** spectra exhibit excellent agreement with the Dke1-acac^{X} absorption data, while the 6C **1-acac** spectrum is nearly identical to the one reported for HPPD-acac.[49] Thus, while our results indicate that the ^{R}TIP ligands accurately reproduces the enzymatic 3His coordination environment, they would also seem to corroborate the conclusion of Diebold *et al.* that variations in the facial triad give rise to only modest spectral perturbations.

Yet analysis of the electronic transitions may not provide a complete picture. Our electrochemical results indicate that the **[3-acac^{X}]OTf** complexes are harder to oxidize than the corresponding **2-acac^{X}** complexes by an average of 145 mV, even though the two sets exhibit similar absorption energies. Thus, the charge of the supporting ligand

has a significant impact on the redox potential of the Fe center – a crucial parameter in tuning the O_2 reactivity of the Fe-acac^X unit. These experimental results are consistent with DFT calculations that indicate a sizable stabilization of the Fe d-orbital manifold in the ^{Ph}TIP complexes relative to the ^{Ph2}Tp complexes (*vide supra*). Of course, the Fe redox potential is somewhat irrelevant if the catalytic cycle proceeds via direct reaction of O_2 with the bound acac ligand, as suggested by Straganz;[33] our results, however, cast some doubts on this possibility. Firstly, the proposed mechanism would require significant spin delocalization from the Fe center to the acac^X ligand to overcome the spin-forbidden nature of concerted reaction with O_2. While such a scenario has been shown to occur in Fe^{3+}-containing intradiol catechol dioxygenases,[34,35] our DFT calculations indicate that only a small amount of unpaired spin-density resides on the acac^X ligands in our models. Secondly, the highest-occupied MO of the coordinated acac ligand, which would play a central role in the electrophilic attack of O_2, is at least 1.0 eV lower in energy than the Fe-based MOs in all DFT models. Even for complexes with electron-rich acac ligands, the frontier MOs are exclusively Fe-based, suggesting that reaction with O_2 is more likely at Fe than the ligand. Regardless, further biochemical and synthetic studies are required in order to fully understand the significance of the 3His triad for enzymatic function.

2.G. Experimental Section

Materials. All reagents and solvents were purchased from commercial sources and used as received unless otherwise noted. acetonitrile (MeCN), dichloromethane (DCM), and tetrahydrofuran (THF) were purified and dried using a Vacuum Atmospheres solvent purification system. The supporting ligands were prepared

according to literature procedures.[55] The synthesis and handling of air-sensitive complexes were carried out under inert atmospheres using custom built Schlenk lines and a Vacuum Atmospheres Omni-Lab glove-box equipped with a freezer set to -30ºC.

Physical Methods. Compounds were characterized and studied using elemental analysis, IR, NMR, UV-Vis, X-ray diffraction, and CV. Elemental analyses were performed at Midwest Microlab, LLC in Indianapolis, Indiana. Infrared spectra were measured as a powder on a Thermo Fisher Scientific Nicolet iS5 FT-IR spectrometer with an iD3 ATR accessory, or as KBr pellets using a Nicolet Magna-IR 560 spectrometer. NMR spectra were collected at room temperature with a Varian 400 MHz spectrometer. UV-Vis spectra were collected with an Agilent 8453 diode array spectrometer. Electrochemical measurements were performed with an Epsilon EC potentiostat (iBAS) under nitrogen atmosphere at a scan rate of 100 mV/s with mM $(NBu_4)PF_6$. A three-electrode cell containing a Ag/AgCl reference electrode, a platinum auxiliary electrode, and a glassy carbon working electrode was employed for cyclic voltammetric measurements.

[Fe(^{Ph}TIP)(acac)]OTf, [1]OTf: Sodium methoxide (0.0513 g, 0.9496 mmol) was added to acac (0.0980 g, 0.9788 mmol) in 2 mL of THF and allowed to stir for 30 minutes, after which the solvent was removed under vacuum to yield the Na^+acac^- salt. All reagents were placed into a nitrogen atmosphere glove-box. ^{Ph}TIP (0.4296 g, 0.9330 mmol), anhydrous iron triflate (0.3316 g, 0.9368 mmol), and the Na^+acac^- salt were each dissolved in 3 mL of methanol. The ^{Ph}TIP solution was added dropwise to the iron triflate solution, then the Na^+acac^- salt dropwise to the mixture, resulting in a yellow solution. The mixture was allowed to stir overnight. The solvent was then removed by vacuum and the solid dissolved in 5 mL of MeCN. After filtration to remove insoluble particles, the

solution was cooled to -30°C and yellow crystals formed after several days. Yield: 0.2569g, 36.02%. Anal. Calcd. for $C_{33}H_{28}N_6F_3FeO_5PS$: C, 51.84; H, 3.69; N, 10.99. Found: C, 51.52; H, 3.65; N, 10.68. UV-Vis [λ_{max}, nm (ε, $M^{-1}cm^{-1}$) in MeCN]: 415 (160), 351 (sh). IR (KBr, cm^{-1}): 3207, 1587 [ν(CO)], 1559, 1516, 1478, 1458, 1389.

[Fe(^{Ph}TIP)(acac^{F3})]OTf, [2]OTf: Sodium methoxide (0.0334 g, 0.6183 mmol) was added to acac^{F3} (0.0941 g, 0.6107 mmol) in 2 mL of THF and allowed to stir for 30 minutes, after which the solvent was removed under vacuum to yield the Na^+acac^{F3-} salt. All reagents were placed into a nitrogen atmosphere glove-box. ^{Ph}TIP (0.2694 g, 0.5850 mmol), anhydrous iron triflate (0.2087 g, 0.5896 mmol), and the Na^+acac^{F3-} salt were each dissolved in 3 mL of methanol. The ^{Ph}TIP solution was added dropwise to the iron triflate solution, then the Na^+acac^{F3-} salt dropwise to the mixture, resulting in an orange solution. The mixture was allowed to stir overnight. The solvent was then removed under vacuum and the solid dissolved in 5 mL of DCM. After filtration to remove insoluble particles, the solution was layered with pentane, providing orange crystals. Anal. Calcd for $C_{33}H_{25}N_6F_6FeO_5PS$: C, 48.43; H, 3.08; N, 10.27. Found: C, 48.05; H, 3.24; N, 10.04. UV-Vis [λ_{max}, nm (ε, $M^{-1}cm^{-1}$) in MeCN]: 461 (220), 373 (sh). IR (KBr, cm^{-1}): 3221, 1630 [ν(CO)], 1559, 1478, 1458.

[Fe(^{Ph}TIP)(acac^{PhF3})]OTf, [3]OTf: Sodium methoxide (0.0358 g, 0.6627 mmol) was added to acac^{PhF3} (0.1447 g, 0.6694 mmol) in 2 mL of THF and allowed to stir for 30 minutes, after which the solvent was removed under vacuum to yield the Na^+acac^{PhF3-} salt. All reagents were placed into a nitrogen atmosphere glove-box. ^{Ph}TIP (0.2986 g, 0.6484 mmol), anhydrous iron triflate (0.2303 g, 0.6506 mmol), and the Na^+acac^{PhF3-} salt were each dissolved in 3 mL of methanol. The ^{Ph}TIP solution was added dropwise to the iron triflate solution, then the Na^+acac^{PhF3-} salt dropwise to the mixture, resulting in a

reddish-purple solution. The mixture was allowed to stir overnight. The solvent was then removed under vacuum and the solid dissolved in 5 mL of DCM. After filtration to remove insoluble particles, the solution was layered with pentane, providing reddish crystals. Anal. Calcd for $C_{38}H_{27}N_6F_6FeO_5PS$: C, 51.83; H, 3.09; N, 9.54. Found: C, 50.30; H, 3.18; N, 9.13 (the slight discrepancy in the carbon value indicates that small amounts of impurities are present). UV-Vis [λ_{max}, nm (ε, $M^{-1}cm^{-1}$) in MeCN]: 528 (630), 408 (320). IR (KBr, cm^{-1}): 3223, 1609 [ν(CO)], 1574, 1478, 1457.

[Fe(^{Ph}TIP)(acac^{F6})]OTf, [4]OTf: Sodium methoxide (0.0365 g, 0.6757 mmol) was added to acac^{F6} (0.1381 g, 0.6638 mmol) in 2 mL of THF and allowed to stir for 30 minutes, after which the solvent was removed under vacuum to yield the Na^+acac^{F6-} salt. All reagents were placed into a nitrogen atmosphere glove-box. ^{Ph}TIP (0.3021 g, 0.6560 mmol), anhydrous iron triflate (0.2353 g, 0.6647 mmol), and the Na^+acac^{F6-} salt were each dissolved in 3 mL of methanol. The ^{Ph}TIP solution was added dropwise to the iron triflate solution, then the Na^+acac^{F6-} salt dropwise to the mixture, resulting in a purple solution. The mixture was allowed to stir overnight. The solvent was then removed under vacuum and the solid dissolved in 5 mL of DCM. After filtration to remove insoluble particles, the solution was layered with pentane, providing purple crystals. Yield: 0.1462g, 25.54%. Anal. Calcd for $C_{33}H_{22}N_6F_9O_5PSFe$: C, 45.43; H, 2.54; N, 9.63. Found: C, 43.19; H, 2.80; N, 9.32 (the minor discrepancy in the carbon value indicates that small amounts of impurities are present). UV-Vis [λ_{max}, nm (ε, $M^{-1}cm^{-1}$) in MeCN]: 509(450), 381(390). IR (KBr, cm^{-1}): 3206, 1632 [ν(CO)], 1560, 1480.

[Fe(^{tBu}TIP)(acac)]OTf, [5]OTf: Sodium methoxide (0.0287 g, 0.5313 mmol) was added to acac (0.0511 g, 0.5104 mmol) in 2 mL of THF and allowed to stir for 30 minutes, after which the solvent was removed under vacuum to yield the Na^+acac^- salt.

All reagents were placed into a nitrogen atmosphere glove-box. ^{tBu}TIP (0.1965 g, 0.4906 mmol), anhydrous iron triflate (0.1746 g, 0.04932 mmol), and the Na^+acac^- salt were each dissolved in 3 mL of methanol. The ^{tBu}TIP solution was added dropwise to the iron triflate solution, then the Na^+acac^- salt dropwise to the mixture, resulting in a yellow solution. The mixture was allowed to stir overnight. The solvent was then removed under vacuum and the solid dissolved in 5 mL of DCM. After filtration to remove insoluble particles, the solution was cooled to -30°C and yellow crystals formed after several days. UV-Vis [λ_{max}, nm (ε, $M^{-1}cm^{-1}$) in MeCN]: 357 (320), 419 (290).

[Fe(^{tBu}TIP)(acac^{F3})]OTf, [6]OTf: Sodium methoxide (0.0205 g, 0.3795 mmol) was added to acac^{F3} (0.0602 g, 0.3907 mmol) in 2 mL of THF and allowed to stir for 30 minutes, after which the solvent was removed under vacuum to yield the Na^+acac^{F3-} salt. All reagents were placed into a nitrogen atmosphere glove-box. ^{tBu}TIP (0.1513 g, 0.3778 mmol), anhydrous iron triflate (0.1377g, 0.3890 mmol), and the Na^+acac^- salt were each dissolved in 3 mL of methanol. The ^{tBu}TIP solution was added dropwise to the iron triflate solution, then the Na^+acac^{F3-} salt dropwise to the mixture, resulting in an orange solution. The mixture was allowed to stir overnight. The solvent was then removed under vacuum and the solid dissolved in 5 mL of DCM. After filtration to remove insoluble particles, the solution was layered with pentane, providing orange crystals. Anal. Calcd for $C_{27}H_{37}N_6F_6FeO_3PS$: C, 42.76; H, 4.92; N, 11.08. Found: C, 44.85; H, 5.14; N, 12.00 (the minor discrepancy in the carbon value indicates that small amounts of impurities are present). UV-Vis [λ_{max}, nm (ε, $M^{-1}cm^{-1}$) in MeCN]: 360 (sh), 444 (320).

[Fe(^{tBu}TIP)(acac^{PhF3})]OTf, [7]OTf: Sodium methoxide (0.0308 g, 0.5702 mmol) was added to acac^{PhF3} (0.1182 g, 0.5468 mmol) in 2 mL of THF and allowed to stir for 30 minutes, after which the solvent was removed under vacuum to yield the Na^+acac^{PhF3-}

salt. All reagents were placed into a nitrogen atmosphere glove-box. ^{tBu}TIP (0.2158 g, 0.5388 mmol), anhydrous iron triflate (0.1954 g, 0.5520 mmol), and the $Na^{+}acac^{PhF3-}$ salt were each dissolved in 3 mL of methanol. The ^{tBu}TIP solution was added dropwise to the iron triflate solution, then the $Na^{+}acac^{PhF3-}$ salt dropwise to the mixture, resulting in a reddish solution. The mixture was allowed to stir overnight. The solvent was then removed under vacuum and the solid dissolved in 5 mL of DCM. After filtration to remove insoluble particles, the solution was cooled to -30°C and reddish crystals formed after several days. UV-Vis [λ_{max}, nm (ε, $M^{-1}cm^{-1}$) in MeCN]: 390 (sh), 514 (650).

[Fe(^{tBu}TIP)($acac^{F6}$)]OTf, [8]OTf: Sodium methoxide (0.0304 g, 0.5628 mmol) was added to $acac^{F6}$ (0.0.1206 g, 0.5796 mmol) in 2 mL of THF and allowed to stir for 30 minutes, after which the solvent was removed under vacuum to yield the $Na^{+}acac^{F6-}$ salt. All reagents were placed into a nitrogen atmosphere glove-box. ^{tBu}TIP (0.2185 g, 0.5456 mmol), anhydrous iron triflate (0.1963 g, 0.5546 mmol), and the $Na^{+}acac^{F6-}$ salt were each dissolved in 3 mL of methanol. The ^{tBu}TIP solution was added dropwise to the iron triflate solution, then the $Na^{+}acac^{F6-}$ salt dropwise to the mixture, resulting in a purple solution. The mixture was allowed to stir overnight. The solvent was then removed under vacuum and the solid dissolved in 5 mL of DCM. After filtration to remove insoluble particles, the solution was cooled to -30°C and purple crystals formed after several days. UV-Vis [λ_{max}, nm (ε, $M^{-1}cm^{-1}$) in MeCN]: 381 (410), 510 (480).

Crystallographic Studies. Complexes were characterized using X-Ray crystallography. The X-ray diffraction data were collected at 100 K with an Oxford Diffraction SuperNova kappa-diffractometer equipped with dual microfocus Cu/Mo X-ray sources, X-ray mirror optics, Atlas CCD detector and low temperature Cryojet device. Crystallographic data for the compounds are provided in Table 2.9-10. The data

were processed with the CrysAlisPro program package (Oxford Diffraction Ltd., 2010) typically using a numerical Gaussian absorption correction (based on the real shape of the crystal) followed by an empirical multi-scan correction using the SCALE3 ABSPACK routine. The structures were solved using the SHELXS program and refined with the SHELXL program[56] within the Olex2 crystallographic package.[57] All computations were performed on an Intel PC computer with Windows 7 OS. The majority of the structures contain a certain degree of disorder that was detected in difference Fourier syntheses of electron density and accounted for using capabilities of the SHELX package. In most cases, hydrogen atoms were localized in difference syntheses of electron density but were refined using appropriate geometric restrictions on the corresponding bond lengths and bond angles within a riding/rotating model (torsion angles of methyl hydrogens were optimized to better fit the residual electron density).

Density Functional Theory (DFT) Calculations. DFT calculations were performed using the ORCA 2.7 software package developed by Dr. F. Neese.[58] In each case, the corresponding X-Ray structure provided the starting point for geometry optimizations and the computational model included the entire complex (excluding counteranions and uncoordinated solvent molecules). Geometry optimizations employed the Becke-Perdew (BP86) functional[59,60] and Ahlrichs' valence triple-ζ basis set (TZV) for all atoms, in conjunction with the TZV/J auxiliary basis set.[61,62] Extra polarization functions were used on non-hydrogen atoms. Single-point (SP) calculations involving the optimized models were carried out with Becke's three-parameter hybrid functional for exchange along with the Lee-Yang-Parr correlation functional (B3LYP).[63-65] These SP calculations also utilized the TZV basis set noted above, but additional polarization functions were included for all atoms, including hydrogens. The same enlarged basis set

was used for TD-DFT calculations,[66-68] which computed absorption energies and intensities within the Tamm-Dancoff approximation.[69,70] In each case, at least 20 excited states were calculated. Finally, the gOpenMol program[71] developed by Laaksonen was used to generate isosurface plots of molecular orbitals.

Table 2.9. Summary of X-ray crystallographic data collection and structure refinement of **3-acac^{X}**

	[3-acac]OTf ●MeCN	**[3-acac^{F3}]**OTf ●DCM	**[3-acac^{PhF3}]**OTf ●4DCM	**[3-acac^{F6}]**OTf ●2MeCN
empirical formula	$C_{35}H_{31}F_3FeN_7O_5PS$	$C_{34}H_{27}Cl_2F_6FeN_6O_5PS$	$C_{42}H_{35}Cl_8F_6FeN_6O_5PS$	$C_{39}H_{31}F_9FeN_9O_5PS$
formula weight	805.55	903.40	1220.24	995.61
crystal system	triclinic	triclinic	triclinic	orthorhombic
space group	*P-1*	*P-1*	*P-1*	*P*na2_1
a, Å	10.8489(3)	10.9737(3)	11.4327(3)	20.3397(3)
b, Å	12.6264(3)	12.6383(3)	12.8330(2)	11.83101(16)
c, Å	14.4290(4)	14.6113(3)	17.9561(3)	17.8160(2)
α, °	87.443(2)	85.8015(19)	85.0393(15)	90
β, °	71.223(2)	71.277(2)	78.0672(17)	90
γ, °	89.004(2)	87.183(2)	83.3042(17)	90
V, Å^3	1869.46(8)	1913.32(8)	2554.66(9)	4287.23(10)
Z	2	2	2	4
D_{calc}, g/cm^3	1.431	1.568	1.586	1.542
λ, Å	0.7107	0.7107	1.5418	0.7107
μ, mm^{-1}	0.568	0.709	7.525	0.532
θ-range, °	2 to 29	2 to 29	2 to 74	3 to 29
reflections collected	42236	86437	23048	41132
independent reflections	9554 [R_{int} = 0.0335]	10144 [R_{int} = 0.0498]	10023 [R_{int} = 0.0542]	10734 [R_{int} = 0.0251]
data/restraints/ parameters	9554 / 0 / 481	10144 / 26 / 584	10023 / 0 / 631	10734 / 1 / 590
GOF (on F^2)	1.041	1.081	1.033	1.06
R1/wR2 ($I>2\sigma(I)$)[a]	0.0356 / 0.0797	0.0351 / 0.0998	0.0630 / 0.1744	0.0247 / 0.0581
R1/wR2 (all data)	0.0486 / 0.0868	0.0477 / 0.1036	0.0671 / 0.1810	0.0292 / 00589

[a] $R1 = \Sigma||F_o| - |F_c|| / \Sigma|F_o|$; $wR2 = [\Sigma w(F_o^2-F_c^2)^2 / \Sigma w(F_o^2)^2]^{1/2}$

Table 2.10. Summary of X-ray crystallographic data collection and structure refinement **4-acac^{X}**

	[4-acac]OTf●2DCM	**[4-acac^{F3}]**OTf●1.5DCM
empirical formula	$C_{29}H_{44}Cl_4F_3FeN_6O_5PS$	$C_{28.5}H_{40}Cl_3F_6FeN_6O_5PS$
formula weight	874.38	885.89
crystal system	monoclinic	orthorhombic
space group	$P2_1/n$	Pbca
a, Å	15.9204(3)	16.6708(2)
b, Å	15.2548(2)	18.6542(2)
c, Å	16.8867(3)	51.2129(7)
α, °	90	90
β, °	104.1835(18)	90
γ, °	90	90
V, Å^3	3976.13(12)	15926.2(4)
Z	4	16
D_{calc}, g/cm^3	1.461	1.478
λ, Å	0.7107	1.54
μ, mm^{-1}	0.799	6.400
θ-range, °	3 to 60	3 to 71
reflections collected	57294	61315
independent reflections	10301 [R_{int} = 0.0298]	15070 [R_{int} = 0.0612]
data/restraints/ parameters	10301 / 15 / 490	15070 / 0 / 948
GOF (on F^2)	1.031	0.937
R1/wR2 ($I>2\sigma(I)$)[a]	0.0407 / 0.0966	0.0467, 0.1168
R1/wR2 (all data)	0.0532 / 0.1067	0.0622, 0.1216

[a] $R1 = \Sigma||F_o| - |F_c|| / \Sigma|F_o|$; $wR2 = [\Sigma w(F_o^2-F_c^2)^2 / \Sigma w(F_o^2)^2]^{1/2}$

Table 2.11. Selected bond distances (Å) and angles (deg) for **1-acac^{X}** complexes.

Bond Distance	[Fe(^{Me2}Tp)(acac)] ●2MeCN	[Fe(^{Me2}Tp)(acac^{F3})] ●MeCN	[Fe(^{Me2}Tp)(acac^{PhF3}] ●MeCN	[Fe(^{Me2}Tp)(acac^{F6})]
Fe-O1	2.0882(8)	2.0563(10)	2.0644(11)	2.1116(6)
Fe-O2	2.0510(8)	2.0843(10)	2.0730(11)	2.0976(6)
Fe-N1	2.1535(9)	2.1798(12)	2.1436(13)	2.1502(7)
Fe-N2	2.1851(9)	2.1353(11)	2.1635(13)	2.1154(7)
Fe-N3	2.1748(9)	2.2141(11)	2.1695(13)	2.1461(7)
Fe-N4	2.2363(10)	2.2212(12)	2.2550(14)	2.2461(7)
Fe-O_{acac}(ave)	2.070	2.070	2.069	2.105
Fe-N_{TIP}(ave)	2.171	2.176	2.158	2.137
Bond Angle				
Fe-N7-C [a]	159.30(9)	161.20(12)	171.49(14)	169.23(7)
acac^{X} tilt [b]	20.0	10.7	18.4	24.4

[a] The atoms consisting the N7-C moiety are in the bound MeCN.
[b] acac^{X} tilt = average angle between the plane of the acac ligand and a plane defined be the O1-Fe-O2 atoms.

Table 2.12. Selected bond distances (Å) and angles (deg) for **2-acac^{X}** complexes.

Bond Distance(Å)	[Fe(^{Ph2}Tp)(acac)]	[Fe(^{Ph2}Tp)(acac^{tBu})] ●0.5MeCN ●0.5THF	[Fe(^{Ph2}Tp)(acac^{F3})] ●DCM	[Fe(^{Ph2}Tp)(acac^{PhF3})] ●DCM
Fe-O1	1.9945(10)	2.0492(13)	2.050(3)	2.054(3)
Fe-O2	2.0239(9)	1.9443(14)	1.956(3)	1.967(3)
Fe-N1	2.1625(10)	2.0945(14)	2.096(3)	2.092(3)
Fe-N3	2.1462(11)	2.2603(15)	2.178(3)	2.231(3)
Fe-N5	2.0984(9)	2.1074(14)	2.117(3)	2.095(3)
Fe-O_{acac}(ave)	2.009	1.997	2.018	2.011
Fe-N_{Tp}(ave)	2.136	2.154	2.130	2.139
Bond Distance(Å)				
Fe-O1	1.9945(10)	2.0492(13)	2.050(3)	2.054(3)
Fe-O2	2.0239(9)	1.9443(14)	1.956(3)	1.967(3)
Fe-N1	2.1625(10)	2.0945(14)	2.096(3)	2.092(3)
Fe-N3	2.1462(11)	2.2603(15)	2.178(3)	2.231(3)
Fe-N5	2.0984(9)	2.1074(14)	2.117(3)	2.095(3)
O2-Fe-N3	92.64(4)	93.35(6)	92.26(12)	91.01(11)
O2-Fe-N5	103.37(4)	125.96(6)	115.49(13)	122.84(12)
N1-Fe-N3	81.71(4)	82.95(6)	83.07(12)	84.65(11)
N1-Fe-N5	91.31(4)	92.70(5)	91.21(12)	92.19(12)
N3-Fe-N5	89.94(4)	86.23(5)	89.83(11)	86.86(11)
τ-value [a]	0.094	0.607	0.327	0.554

[a] The geometric parameter τ is defined as $\tau = |(\alpha - \beta)|/60$, where α and β are the two basal angles in pseudo-square pyramidal geometry. The τ-value in 0.0 in idealized square-planar geometries and 1.0 in idealized trigonal bipyramidal geometries.[54]

Chapter 3

Synthesis and Structural Characterization of Iron(II) Complexes with Tris(imidazolyl)phosphane Ligands: A Platform for Modeling the 3-Histidine Facial Triad of Salicylate Dioxygenase

Abstract: Two monoiron(II) complexes containing the tris(2-phenylimidazol-4-yl)phosphane (^{Ph}TIP) ligand have been prepared and structurally characterized with X-ray crystallography and NMR spectroscopy. The ^{Ph}TIP framework resembles the 3-histidine (3His) facial triad found recently in the active sites of certain nonheme iron dioxygenases. The complex [Fe^{2+}(^{Ph}TIP)(OAc)(MeOH)]BPh_4, **[1]**BPh_4, was designed to serve as a convenient precursor to species that model the enzyme-substrate intermediates of 3His dioxygenases. The viability of this approach was demonstrated through the synthesis of [Fe^{2+}(^{Ph}TIP)(sal)] (**2**; sal = dianion of salicylic acid) that represents the first synthetic model of the enzyme salicylate 1,2-dioxygenase (SDO).

3.A. Introduction

Mononuclear nonheme iron dioxygenases play a central role in the oxidative catabolism of a wide range of biomolecules and pollutants.[5,17,72] Members of this enzyme family include the extradiol catechol dioxygenases,[14,73,74] Rieske dioxygenases,[8] homogentisate dioxygenase,[9] and (chloro)hydroquinone dioxygenases.[44-47] These enzymes feature a common active-site motif in which the ferrous center is facially ligated by one aspartate (or glutamate) and two histidine residues (the so-called 2-His-1-carboxylate (2H1C) facial triad).[13] However, recent structural studies have shown that the Asp/Glu ligand in some monoiron dioxygenases is replaced with His, resulting in the 3His facial triad.[18,19] Members of this "3His family" catalyze novel transformations that have expanded the known boundaries of Fe dioxygenase chemistry. For example, cysteine dioxygenase (CDO)[21] – the first 3His enzyme to be structurally characterized – catalyzes the initial step in L-cysteine catabolism by converting the thiol into a sulfinic acid (Scheme 3.1), while β-diketone dioxygenase (Dke1) oxidizes acetylacetone to acetic acid and 2-oxopropanal.[26] Other 3His Fe dioxygenases include gentisate 1,2-dioxygenase (GDO)[27] and salicylate 1,2-dioxygenase (SDO),[28,29] both of which oxidatively cleave aromatic C-C bonds (Scheme 3.1). Each of these microbial enzymes participates in the degradation pathways of polycyclic aromatic hydrocarbons. While the reaction catalyzed by GDO is very similar to those catalyzed by the extradiol catechol dioxygenases and likely follows a similar mechanism, SDO is unique in performing the oxidative cleavage of an aromatic ring with only one electron-donating group.

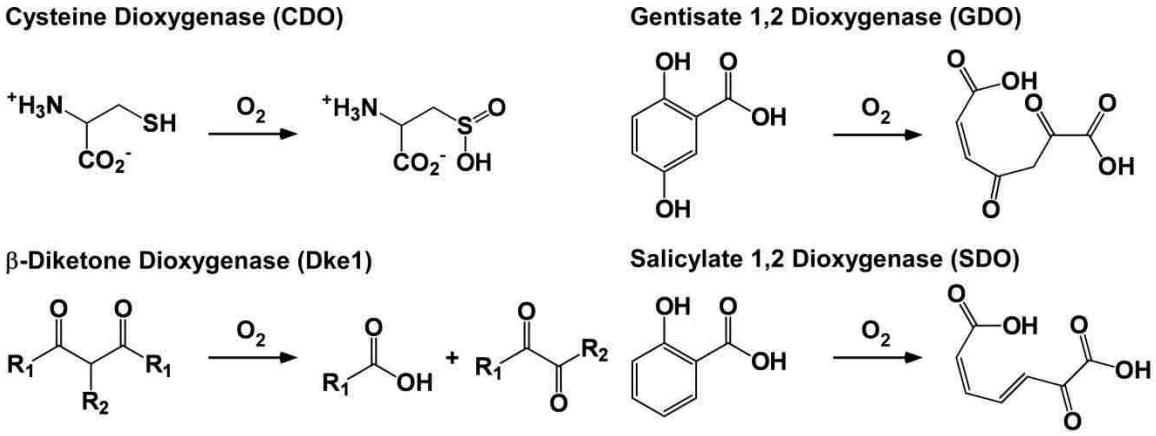

Scheme 3.1.

Our knowledge of nonheme Fe dioxygenases has greatly benefited from the development of small-molecule analogs that replicate important structural, spectroscopic, and/or functional properties of the enzyme active sites.[15] The 2H1C triad has been suitably modeled with tridentate supporting ligands such as tris(pyrazol-1-yl)borates (Tp),[46,48] 1,4,7-triazacyclononane (tacn),[79,80] bispyrazolylacetates,[81,82] and bis(1-alkylimidazol-2-yl)propionates.[43] Given the unique and significant reactions catalyzed by the 3His family of Fe dioxygenases, it is important to develop supporting ligands with specific relevance to the 3His facial triad. To this end, we have sought to exploit the tris(imidazol-4-yl)phosphane (^{R}TIP) framework shown in Scheme 3.2, which accurately mimics the charge and donor strength of the 3His coordination environment. Such ligands were initially generated to model the 3His ligand sets found in the active sites of carbonic anhydrase (Zn^{2+}) and cytochrome *c* oxidase (Cu^{2+}).[55,83-88] To date, the application of the TIP framework to Fe systems has been limited to homoleptic $[Fe(TIP)_2]^{2+/3+}$ complexes[89-91] and carboxylate-bridged diiron(III) species.[91-93]

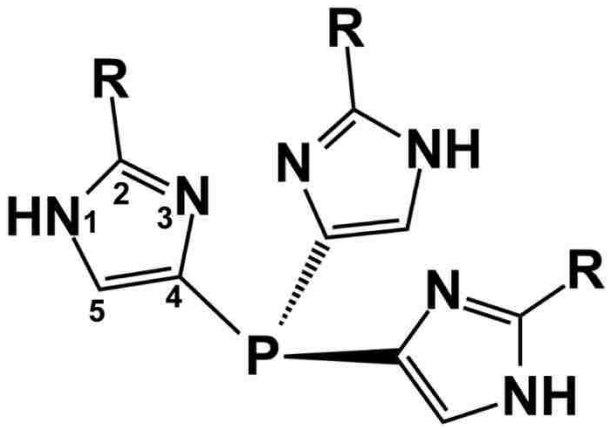

Scheme 3.2.

A key advantage of ^{R}TIP ligands is that their steric properties can be easily modified by altering the R-substituent. Thus far, we have primarily employed the ^{Ph}TIP ligand, as the steric bulk of the phenyl rings discourages both dimerization and formation of the homoleptic $[Fe(TIP)_2]^{2+}$ complexes. In Chapter 2, we described the synthesis and structural characterization of a series of $[Fe^{2+}(^{Ph}TIP)(acac^{X})]OTf$ complexes that serve as models of the Dke1 enzyme-substrate complex ($acac^{X}$ = substituted β-diketonate). These models were prepared by directly mixing one equivalent of the sodium salt of the appropriate β-diketone, $Na(acac^{X})$, with equimolar amounts of $Fe(OTf)_2$ and ^{Ph}TIP in MeOH. This "one-pot" approach, however, is not successful for various combinations of supporting and "substrate" ligands. Thus, as described in this article, we have generated an Fe^{2+} complex (**[1]**BPh_4) with ^{Ph}TIP that contains displaceable ligands (solvent and acetate) bound to the opposite face of the octahedron. This complex resembles the resting states of 3His Fe dioxygenases, which feature two or three *cis*-labile H_2O molecules.[24,25] In addition, it is shown that **[1]**BPh_4 serves as an excellent precursor for the formation of a synthetic mimic of SDO. Thus, the chemistry described here establishes a valuable platform for future synthetic modeling studies of nonheme Fe dioxygenases with the 3His facial triad.

3.B. Synthesis and Solid State Structures

The complex $[Fe^{2+}(^{Ph}TIP)(OAc)(MeOH)]BPh_4$, **[1]**$BPh_4$, was generated by addition to $NaBPh_4$ to a solution of $Fe(OAc)_2$ and ^{Ph}TIP in MeOH, resulting in immediate formation of a white precipitate. The IR spectrum of the isolated solid reveals a peak at 3259 cm^{-1} from the ν(N-H) stretch of the ^{Ph}TIP ligands, along with acetate-derived features at 1562 and 1402 cm^{-1}. The ^{Ph}TIP-derived resonances in the ^1H NMR spectrum largely follow the pattern reported previously for $[Fe^{2+}(^{Ph}TIP)(acac^X)]^+$ complexes. The acetate ligand of **[1]**BPh_4 exhibits a downfield signal at +105 ppm.

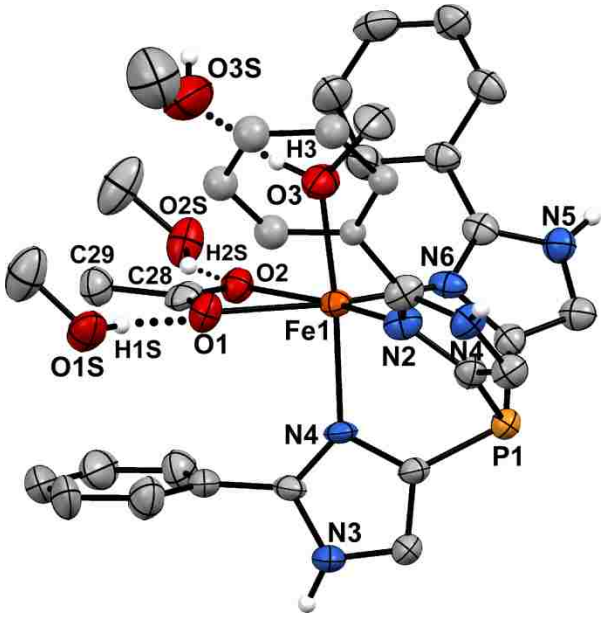

Figure 3.1. Thermal ellipsoid plot (50% probability) derived from **[1]**BPh_4●3MeOH. The BPh_4 counteranion and most hydrogen atoms have been omitted for clarity. The dotted lines signify the hydrogen-bonding interactions between the coordinated acetate and the MeOH ligands and three second-sphere solvent molecules. Note: Ellipsoids are not shown for the proximal 2-phenyl substituent due to disorder.

X-ray quality crystals of **[1]**BPh_4 were prepared via slow-cooling of a MeOH solution; the $\mathbf{[1]}^+$ cation is shown in Figure 3.1 and the corresponding bond lengths and

angles are provided in Table 3.1. The high-spin Fe(II) center is hexacoordinate with a facially-coordinating ^{Ph}TIP ligand. The κ^2-acetate ligand coordinates in a symmetric manner with nearly identical Fe-$O_{acetate}$ distances of 2.251(6) Å. The remaining site is occupied by a solvent molecule *trans* to N4 with a relatively short Fe-O_{MeOH} distance of 2.077(4) Å. The crystal structure of **[1]**BPh_4•3MeOH also features an extensive H-bonding network. As shown in Figure 3.1, the coordinated acetate and MeOH moieties participate in H-bonding interactions with three MeOH "chaperones" that comprise a second-sphere shell surrounding one face of the $\mathbf{[1]}^+$ octahedron. In addition, the MeOH molecules that serve as H-bond *donors* to the acetate ligand also act as H-bond *acceptors* for two H-$N_{imidazole}$ groups on adjacent $\mathbf{[1]}^+$ cations.

Significantly, we found that **[1]**BPh_4 provides access to iron(II)-salicylate (sal) species that mimic the enzyme-substrate complex of SDO. The complex [Fe(^{Ph}TIP)(sal)] (**2**) was prepared by mixing **[1]**BPh_4 with one equivalent of sodium salicylate in MeOH, followed by layering with MeCN. As shown in Figure 3.2, the X-ray crystal structure of **2** reveals a neutral 5C Fe(II) complex with a geometry intermediate between square pyramidal and trigonal bipyramidal (τ = 0.35). The dianionic salicylate ligand coordinates in a bidentate fashion with Fe–O bond distances of 1.958(1) and 2.060(1) Å for the phenolate and carboxylate donors, respectively. To the best of our knowledge, **2** represents the first structurally-characterized iron(II)-salicylate complex in the chemical literature.[94-97]

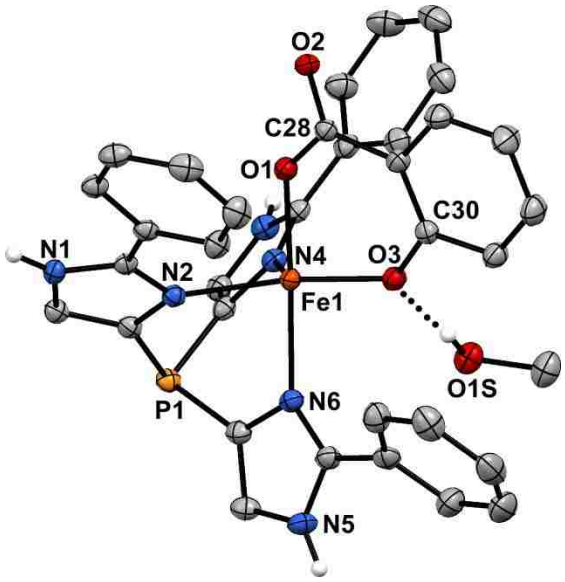

Figure 3.2 Thermal ellipsoid plot (50% probability) derived from **2**●MeOH●MeCN. The noncoordinating solvent molecules and most hydrogen atoms have been omitted for clarity. The dotted line represents the H-bonding interaction between the salicylate ligand and MeOH.

As with [**1**]BPh_4•3MeOH, the lattice of **2** exhibits numerous H-bonding interactions (see Scheme 3.3). The uncoordinated oxygen atom of the carboxylate (O2) forms H-bonds with two H-N groups belonging to adjacent 4-TIP^{Ph} ligands. These interactions account for the fact that O2-C28 is unexpectedly *longer* than O1-C28 (1.273(2) vs. 1.257(2), respectively), indicating that the negative charge is delocalized over the carboxylate moiety. The crystal also contains noncoordinating MeCN and MeOH molecules (one of each); the latter serves as a H-bond donor to the phenolate oxygen atom (O3) of the salicylate, while acting as a H-bond acceptor to an imidazole H-N group. Thus, in this structure, the MeOH behaves in a manner similar to second-sphere residues in dioxygenase active sites, which often play a crucial role in stabilizing metal-bound substrates via non-covalent interactions.[36,98]

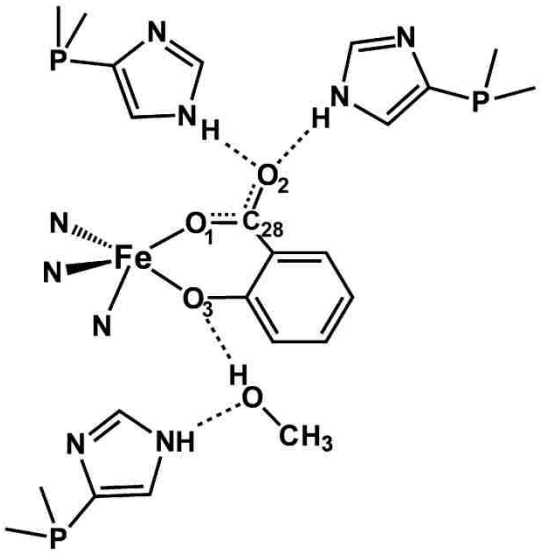

Scheme 3.3. Hydrogen-bonding network in the solid-state structure of **2.**

3.C. Comparisons to the X-ray Structure of SDO.

The X-ray diffraction studies of SDO revealed a homotetrameric structure with four active sites, each composed of an iron(II) center bound to the protein by a facial triad composed of residues His119, His121, and His160. The Fe(II)-N_{His} bond lengths in the four subunits range from 1.85 to 2.31 Å.[28] In two subunits, a single water molecule completes the coordination sphere with Fe-O_{water} distances of 1.93 and 2.55 Å. The third subunit features an acetate ion from the crystallization solvent coordinate in a bidentate, asymmetric fashion with Fe(II)-$O_{acetate}$ bond lengths of 2.53 and 2.91 Å. In the fourth subunit, both acetate and water molecules are found in the vicinity of the Fe center.[28] Thus, complex **[1]**BPh_4 is an excellent model of the SDO resting state.

Computational docking studies of SDO have shown three potential orientations for the bound substrate (Scheme 3.4). In two orientations, the carboxylate group of the salicylate ligand participates in hydrogen-bonding interactions with a nearby Arg127

residue. The extensive hydrogen-bonding network evident in the structure of **2** mimics these interactions with second sphere residues.

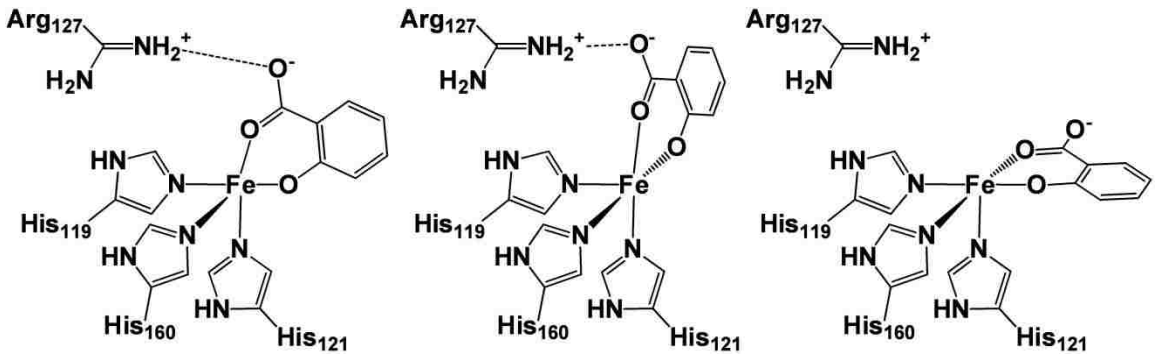

Scheme 3.4.

3.D. Conclusions

This paper has described the synthesis and X-ray structural characterization of iron(II) complexes supported by the tris(imidazolyl)phosphane ligand ^{Ph}TIP. Complex **[1]**BPh_4 features easily-displaced solvent and acetate ligands in the coordination sites *trans* to the TIP chelate. Like the resting states of the enzymatic active sites, this "precursor" complex is intended to serve as a scaffold that permits various substrate ligands to coordinate to the iron(II) center. The versatility of this approach was demonstrated by the formation of the SDO model **2** via direct reaction of [**1**]BPh_4 with sodium salicylate. The facile formation of **2** indicates that the TIP framework is resistant to displacement by strong, anionic ligands. This is significant because half-sandwich ferrous complexes with neutral L_{N3} ligands, such as trispyrazolylmethanes, have been shown to suffer from high lability and a tendency to decompose to the more stable bis-ligand species.[99] The relatively short Fe-N_{TIP} bond distances found in our series of

complexes suggest that the TIP ligands are tightly bind to the iron centers. Thus, the precursor complex described here provides a robust platform for the development of synthetic models of dioxygenases with the 3His facial triad.

3.E. Experimental Section

General Procedures: All reagents and solvents were purchased from commercial sources and used as received unless otherwise noted. MeCN and CH_2Cl_2 were purified and dried using a Vacuum Atmospheres solvent purification system. ^{Ph}TIP was prepared according to literature procedures[55]. The synthesis and handling of air-sensitive materials were carried out under inert atmosphere using a Vacuum Atmospheres Omni-Lab glovebox equipped with a freezer set to -30 ^{o}C. Elemental analyses were performed at Midwest Microlab, LLC in Indianapolis, IN. Infrared (IR) spectra of solid samples were measured with a Thermo Scientific Nicolet iS5 FTIR spectrometer equipped with the iD3 attenuated total reflectance accessory. UV-vis spectra were obtained with an Agilent 8453 diode array spectrometer. Magnetic susceptibility measurements were carried out using the Evans NMR method.

[Fe(4-TIP^{Ph})(OAc)(MeOH)]BPh$_4$ ([1]BPh$_4$): $Fe(OAc)_2$ (488 mg, 2.81 mmol) and ^{Ph}TIP (1.28 g, 2.79 mmol) were stirred in 10 mL of MeOH for 10 minutes while the solution cleared. A solution of $NaBPh_4$ (956 mg, 2.79 mmol) in MeOH was then added dropwise and the mixture stirred for 5 hours. During this time, a white precipitate developed. The white solid was collected and recrystallized from MeOH at -30°C. Yield: 48 % $C_{54}H_{47}BFeN_6O_3P$ (925.6): calcd. C 70.07, H 5.12, N 9.08; found C 70.69, H

5.08, N 8.95. IR (neat): 3304, 3259 [ν(N-H)], 3054, 2999, 2993, 2928, 1562 [ν_{as}(OCO)], 1478, 1402 [ν_{s}(OCO)], 1341 cm^{-1}.

[Fe(4-TIP^{Ph})(sal)] (2): A suspension of **[1]**BPh_4 (142 mg, 0.159 mmol) and sodium salicylate (28.0 mg, 0.175 mmol) was stirred overnight in 5 mL of MeOH. The resulting yellow solution was layered with MeCN to provide X-ray quality crystals of **2**. Yield: 32 %. $C_{34}H_{25}FeN_6O_3P$ (652.4): calcd. C 62.59, H 3.86, N 12.88; found C 62.19, H 3.98, N 12.52. IR (neat): 3133, 3052, 2900, 1598, 1563, 1521, 1476, 1458, 1439, 1386, 1314.

X-ray Structure Determination. X-ray diffraction (XRD) data were collected at 100 K with an Oxford Diffraction SuperNova kappa-diffractometer (Agilent Technologies) equipped with dual microfocus Cu/Mo X-ray sources, X-ray mirror optics, Atlas CCD detector, and low-temperature Cryojet device. Crystallographic data for particular compounds are summarized in Table 3.2. The data were analyzed with the CrysAlis Pro program package (Agilent Technologies, 2011) typically using a numerical Gaussian absorption correction (based on the real shape of the crystal), followed by an empirical multi-scan correction using SCALE3 ABSPACK routine. The structures were solved using SHELXS program and refined with SHELXL program[56] within the Olex2 crystallographic package.[57] H- and C-bonded hydrogen atoms were positioned geometrically and refined using appropriate geometric restrictions on the corresponding bond lengths and bond angles within a riding/rotating model (torsion angles of methyl hydrogens were rotationally optimized to better fit the residual electron density). The positions of the methanolic H-atoms (H3) in **[1]**BPh_4•3MeOH were refined freely. The remaining OH groups were refined using geometrical restrictions and rotationally

optimized to better fit the residual electron density. Crystals of **[1]**BPh_4•3MeOH are systematic twins grown together along a common *bc* plane.

Table 3.1. Selected Bond Distances and Angles.

Bond Distance (Å)	**[1]**BPh_4●3MeOH	**2**●MeOH●MeCN
Fe-O1	2.246(4)	2.0596(9)
Fe-O2	2.256(4)	1.9581(9)
Fe-O3	2.077(4)	-
Fe-N2	2.193(4)	2.1354(11)
Fe-N4	2.195(4)	2.1501(11)
Fe-N6	2.186(4)	2.1826(11)
Fe-$O_{substrate}$(ave)	2.2510	2.0089
Fe-N_{TIP}(ave)	2.1913	2.1560
Bond Angle(°)		
O1-Fe-O2	58.01(13)	86.29(4)
O1-Fe-N2	105.92(14)	92.17(4)
O1-Fe-N4	91.13(15)	96.90(4)
O1-Fe-N6	163.72(14)	168.66(4)
O2-Fe-N2	163.88(14)	147.75(4)
O2-Fe-N4	91.36(14)	117.46(4)
O2-Fe-N6	105.77(14)	91.71(4)
N2-Fe-N4	90.16(15)	94.71(4)
N2-Fe-N6	90.26(16)	83.57(4)
N4-Fe-N6	90.64(14)	93.92(4)
τ-value [a]	N/A	0.348

[a] The geometric parameter τ is defined as $\tau = |(\alpha - \beta)|/60$, where α and β are the two basal angles in pseudo-square pyramidal geometry. The τ-value in 0.0 in idealized square-planar geometries and 1.0 in idealized trigonal bipyramidal geometries.[54]

Table 3.2. Summary of X-ray Crystallographic Data Collection and Structure Refinement

	[1]BPh_4●3MeOH	**2**●MeOH●MeCN
empirical formula	$C_{57}H_{60}BFeN_6O_6P$	$C3_7H_{32}FeN_7O_4P$
formula weight	1022.74	725.52
crystal system	monoclinic	monoclinic
space group	$P2_1$	$P2_1$/n
a, Å	13.8829(3)	13.6187(7)
b, Å	11.6385(4)	14.9164(9)
c, Å	16.5130(4)	17.5278(8)
α, °	90	90
β, °	91.591(2)	102.190(5)
γ, °	90	90
V, $Å^3$	2667.1(2)	3480.4(3)
Z	2	4
D_{calc}, g/cm^3	1.274	1.385
λ, Å	1.5418	1.5418
μ, mm^{-1}	2.996	4.328
ϑ-range, °	4 to 148	4 to 149
reflections collected	32914	26690
independent reflections	10151 [R_{int} = 0.1419]	6954 [R_{int} = 0.0278]
data/restraints/parameters	10151 / 87 / 643	6954 / 0 / 454
GOF (on F^2)	1.025	1.037
R1/wR2 ($I>2\sigma(I)$)[a]	0.0682 / 0.1778	0.0273 / 0.0710
R1/wR2 (all data)	0.0872 / 0.1963	0.0306 / 0.0731

[a] $R1 = \Sigma||F_o| - |F_c|| / \Sigma|F_o|$; $wR2 = [\Sigma w(F_o^2-F_c^2)^2 / \Sigma w(F_o^2)^2]^{1/2}$

Chapter 4

Variations on the Tris(imidazol-4-yl)phosphine Framework

Abstract: An iron and a cobalt complex containing the L_{N3} ligand tris(1-ethylbenzimidazol-2-yl)phosphine (2-TBIP^{Et}) have been prepared and structurally characterized with X-ray crystallography. The 2-TBIP^{Et} framework is similar to that of ^{Ph}TIP and ^{tBu}TIP previously used to model the 3-histidine (3His) facial triad recently found in acetylacetone dioxygenase (Dke1). The complex [Fe^{2+}(2-TBIP^{Et})(acac^{F6})](OTf) ([**1]OTf**) was synthesized to determine whether the lack of O_2 reactivity present in ^{Ph}TIP and ^{tBu}TIP complexes is because of steric or electronic conditions.

4.A. Introduction

Iron(II) β-diketonate complexes with either ^{Ph2}Tp or ^{R}TIP (R = Ph or ^{t}Bu) supporting ligands take several days to oxidize in the presence of dioxygen, whereas the corresponding ^{Me2}Tp complexes readily react with O_2 to yield diiron(III)-peroxo intermediates. To determine whether the lack of reactivity of the TIP-based complexes is due to steric or electronic factors, we attempted to generate the TIP ligands shown in Scheme 4.1, which contain less sterically bulky substituents. In many cases, the synthesis of the ligand was not successful. Tris(1-methylimidazol-2-yl)phosphine (2-TIP^{Me}) could be easily synthesized in large enough quantities; however, due to the lack of steric hindrance, the major product formed upon reaction with one equivalent each of $Fe(OTf)_2$ and Na(acac^{X}) was the homoleptic complex $[Fe(2\text{-}TIP^{Me})_2](OTf)_2$. We therefore turned to tris(1-ethylbenzimidazol-2-yl)phosphine (2-TBIP^{Et}). With this ligand, we were able to generate mononuclear two β-diketonate complexes; this section describes their synthesis and crystallographic characterization.

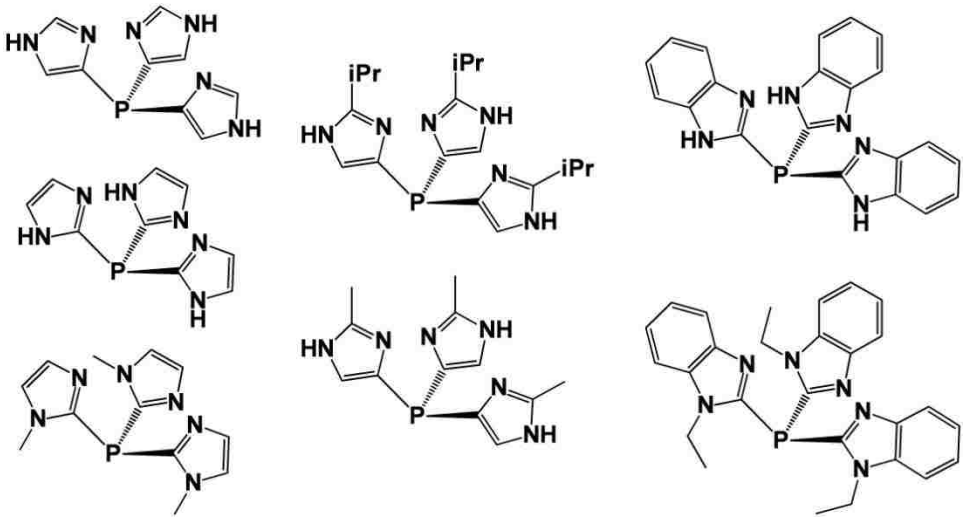

Scheme 4.1. TIP ligands with varying steric and electronic properties.

4.B. Synthesis and Solid-State Structures.

The β-diketonato complexes [Fe(2-TBIP^{Et})(acac^{F6})](OTf) ([**1**]**OTf**) and [Co(2-TBIP^{Et})(acac^{F6})](OTf) ([**2**]**OTf**) were generated via addition of the ligand to MeOH solutions of Na(acac^{F6}) and the appropriate triflate salt. Both complexes were characterized with X-ray crystallography. Selected bond lengths and angles are shown in Table 4.1, while details concerning the data collection and analysis are provided in the Experimental Section (Table 4.2).

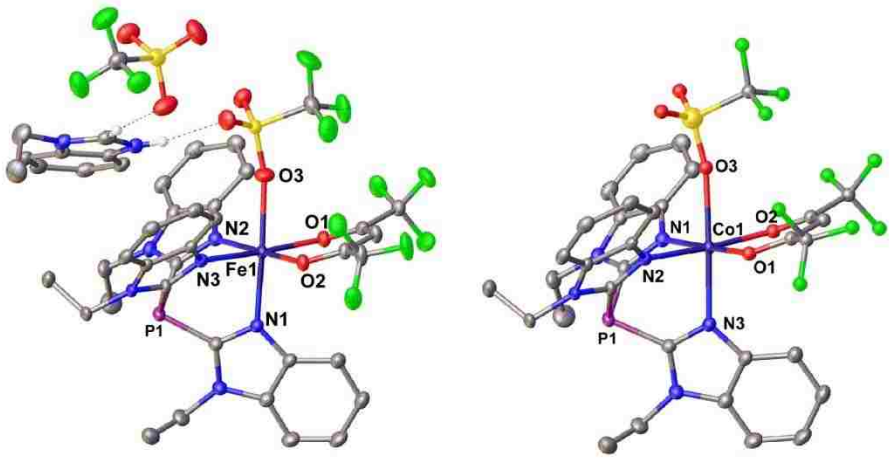

Figure 4.1. Thermal ellipsoid plot (50% probability) derived from **[1]OTf** (left) and **[2]OTf** (right). The noncoordinating solvent molecules and most hydrogen atoms have been omitted for clarity. The dotted line represents the H-bonding interaction between the [BI^{Et}-H]OTf salt. Note: Ellipsoids are not shown for the acac^{F6} and trfilate ligands of **[2]OTf** due to disorder.

X-ray quality crystals of **[1]OTf** were obtained by layering a concentrated CH_2Cl_2 solution with pentane. Attachment of the benzimidazole to the phosphorus at the 2-position allows the three nitrogen donors to coordinate to the metal center, while the

benzene ring modifies the steric hindrance, creating a more open area for the metal center than the ^{Ph}TIP and ^{tBu}TIP ligands. This more open structure of the facially coordinated 2-TBIP^{Et} ligand allows a triflate counteranion to bind to the Fe(II) center, resulting in a distorted octahedral geometry. The average Fe-$N_{benzimid}$ distance of 2.16 Å is similar to the values found for complexes with sterically-hindered TIP ligands. The acac^{F6} ligand bonds symmetrically in a bidentate fashion with an average Fe-O_{acac} distance of 2.06 Å; the Fe-$O_{triflate}$ bond exhibits a distance of 2.2279(15) Å. Interestingly, this complex co-crystallized with one eqiuvalent of [BI^{Et}-H]OTf salt, where BI^{Et}-H is the conjugate acid of 1-ethylbenzimidazole. This second-sphere salt apparently arises from partial degradation of the ^{Et}TBIP ligand. In this case it is somewhat advantageous, since the BI^{Et}-H$^+$ cation stabilizes the inner sphere triflate ion through hydrogen-bonding interactions. The second triflate equivalent in the asymmetric unit also participated in H-bonding interactions with the BI^{Et}-H$^+$ cation.

As with **[1]OTf**, X-ray quality crystals of **[2]OTf** were generated by layering of a DCM solution with pentane. This complex is quite similar to its iron analogue, with the open structure of the 2-TBIP^{Et} ligand permitting coordination of the triflate counterion to the Co(II) center, except with extreme disorder in the positions of the acac^{F6} and the triflate ligands. This problem was compounded by the presence of ~2.5 disordered DCM molecules in the asymmetric unit.

Due to the extreme disorder of **[2]OTf** it is difficult to compare the bond lengths between the two species. The average Co-$N_{benzimid}$ distance is 2.13 Å, shorter than the **[1]OTf**. The oxygens of the acac^{F6} ligand however are indistinguishable from the cobalt

bonded triflate oxygen. The average Co-O distance is 2.11 Å, almost halfway in between the Fe-O_{acac} and Fe-$O_{triflate}$ distances in **[1]OTf.**

Table 4.1. Selected Bond Distances and Angles.

Bond Distance(Å)	**[1]OTf**	**[2]OTf**
Fe-O1	2.0566(14)	2.113(3)
Fe-O2	2.0601(14)	2.113(3)
Fe-O3	2.2279(15)	2.113(3)
Fe-N1	2.1734(16)	2.126(4)
Fe-N2	2.1685(16)	2.126(4)
Fe-N3	2.1424(16)	2.126(4)
Fe-O_{acac}(ave)	2.0584	2.113
Fe-N(ave)	2.1614	2.126
Bond Angle(°)		
O1-Fe-O2	85.87(5)	86.31(12)
O1-Fe-N1	96.96(6)	177.15(13)
O1-Fe-N2	97.48(6)	94.39(13)
O1-Fe-N3	172.67(6)	90.97(13)
O2-Fe-N1	94.90(6)	177.15(13)
O2-Fe-N2	176.12(6)	94.39(13)
O2-Fe-N3	88.50(6)	90.97(13)
N1-Fe-N2	86.65(6)	88.37(14)
N1-Fe-N3	88.19(6)	88.37(14)
N2-Fe-N3	87.99(6)	88.37(14)

4.C. Experimental Section

Materials. All reagents and solvents were purchased from commercial sources and used as received unless otherwise noted. Acetonitrile (MeCN), dichloromethane (DCM), and tetrahydrofuran (THF) were purified and dried using a Vacuum Atmospheres solvent purification system. The supporting ligands were prepared according to literature procedures.[55] The synthesis and handling of air-sensitive complexes were carried out under inert atmospheres using custom built Schlenk lines and a Vacuum Atmospheres Omni-Lab glove-box equipped with a freezer set to -30ºC.

[Fe(2-TBIP^{Et})(acac^{F6})](OTf) [1]OTf: Sodium methoxide (0.0255 g, 0.4720 mmol) was added to acac^{F6} (0.0654 g, 0.3143 mmol) in 2 mL of THF and allowed to stir for 30 minutes, after which the solvent was removed under vacuum to yield the $Na^{+}acac^{F6-}$ salt. All reagents were placed into a nitrogen atmosphere glove-box. ^{Et}TBIP (0.1842 g, 0.3948 mmol) was dissolved in 3 mL DCM while anhydrous iron triflate (0.1430 g, 0.4040 mmol) and the $Na^{+}acac^{F6-}$ salt were each dissolved in 3 mL of methanol. The ^{Et}TBIP solution was added dropwise to the iron triflate solution, then the $Na^{+}acac^{F6-}$ salt dropwise to the mixture, resulting in a purple solution. The mixture was allowed to stir overnight. The solvent was then removed under vacuum and the solid dissolved in 5 mL of DCM. After filtration to remove insoluble particles, he solution was layered with pentane, providing purple crystals.

[Co(2-TBIP^{Et})(acac^{F6})](OTf) [2]OTf: Sodium methoxide (0.0298 g, 0.5516 mmol) was added to acac^{F6} (0.0654 g, 0.3614 mmol) in 2 mL of THF and allowed to stir for 30 minutes, after which the solvent was removed under vacuum to yield the

$Na^{+}acac^{F6-}$ salt. ^{Et}TBIP (0.2246 g, 0.4814 mmol) and cobalt triflate[54] (0.1430 g, 0.4870 mmol) were suspended in 3 mL and the $Na^{+}acac^{F6-}$ salt dissolved in 3 mL of methanol. The ^{Et}TBIP suspension was added dropwise to the anhydrous cobalt triflate suspension, then the $Na^{+}acac^{F6-}$ salt dropwise to the mixture, resulting in a red-orange solution. The mixture was allowed to stir overnight. The solvent was then removed under vacuum and the solid dissolved in 5 mL of DCM. After filtration to remove insoluble particles, the solution was layered with pentane, providing orange crystals.

Crystallographic Studies. Complexes **[1]OTf** and **[2]OTf** were characterized using X-Ray crystallography. The X-ray diffraction data were collected at 100 K with an Oxford Diffraction SuperNova kappa-diffractometer equipped with dual microfocus Cu/Mo X-ray sources, X-ray mirror optics, Atlas CCD detector and low temperature Cryojet device. Crystallographic data for the compounds are provided in Table 4.2. The data were processed with CrysAlisPro program package (Oxford Diffraction Ltd., 2010) typically using a numerical Gaussian absorption correction (based on the real shape of the crystal) followed by an empirical multi-scan correction using the SCALE3 ABSPACK routine. The structures were solved using the SHELXS program and refined with the SHELXL program[56] within the Olex2 crystallographic package.[57] Carbon bonded hydrogen atoms were positioned geometrically and refined using appropriate geometric restrictions on the corresponding bond lengths and angles within a riding/rotating model (torsion angles of methyl hydrogens were rotationally optimized to better fit the residual electron density).

Table 4.2. Summary of X-ray Crystallographic Data Collection and Structure Refinement.

	[1]OTf	**[2]**OTf●2DCM
empirical formula	$C_{43}H_{39}F_{12}FeN_8O_8PS_2$	$C_{33}H_{28}Cl_{4.4}CoF_9N_6O_5PS$
formula weight	1174.76	1037.58
crystal system	monoclinic	trigonal
space group	$P2_1/n$	$P\text{-}3$
a, Å	15.9874(4)	14.8884(8)
b, Å	14.4275(4)	14.8884(8)
c, Å	21.1542(6)	11.8936(6)
α, °	90	90
β, °	95.690(3)	90
γ, °	90	120
V, Å^3	4855.4(2)	2283.2(2)
Z	4	2
D_{calc}, g/cm^3	1.607	1.509
λ, Å	1.5418	1.5418
μ, mm^{-1}	4.573	6.809
θ-range, °	7 to 148	7 to 148
reflections collected	26712	14326
independent reflections	9653 [R_{int} = 0.0284]	3066 [R_{int} = 0.0731]
data/restraints/parameters	9653 / 0 / 684	3066 / 14 / 220
GOF (on F^2)	1.019	1.054
R1/wR2 ($I>2\sigma(I)$)[a]	0.0353 / 0.0926	0.0885 / 0.2456
R1/wR2 (all data)	0.0405 / 0.0969	0.0972 / 0.2551

[a] $R1 = \Sigma||F_o| - |F_c|| / \Sigma|F_o|$; $wR2 = [\Sigma w(F_o^2-F_c^2)^2 / \Sigma w(F_o^2)^2]^{1/2}$

BIBLIOGRAPHY

1. Baker, K.H.; Herson, D.S. *Bioremediation*; Baker, K.H. and Herson, D.S., (Eds.); McGraw-Hill, Inc.: New York, **1994**, 9-60.

2. Singh, A.; Ward, O.P. In *Biodegradation and Bioremediation*; Singh, A. and Ward, O.P, Eds.; Springer: Heidelberg, **2004**, pp 1-18.

3. Parales, R.E.; Haddock, J.D. *Curr. Opin. Biotachnol*. **2004**, *15*, 374-379.

4. Wackett, L.P.; Hershberger, C.D. *Biocatalysis and Biodegradation: Microbial Transformation of Organic Compounds*, ASM Press: Washington, D.C., **2001.**

5. Gibson, D.T.; Pareles, R.E. *Curr. Opin. Biotechnol.* **2000**, *11*, 236-243.

6. Parales, R.; Resnick, S.M. In *Biodegradation and Bioremediation*; Singh, A. and Ward, O.P, Eds.; Springer: Heidelberg, **2004**, pp 175-196.

7. Aitken, M.D.; Long, T.C. *Biodegradation and Bioremediation*; Singh, A. and Ward, O.P, Eds.; Springer: Heidelberg, **2004**, pp 83-124.

8. Kauppi, B.; Lee, K.; Carredano, E.; Parales, R.E.; Gibson, D.T.; Eklund, H.; Ramaswamy, S. *Structure* **1998**, *6*, 571-586.

9. Vaillancourt, F.H.; Bolin, J.T.; Eltis, L.D. *Crit. Rev. Biochem. Mol. Biol.* **2006**, *41*, 241- 267.

10. Lendenmann, U.; Spain, J.C. *J. Bacteriol.* **1996**, *178*, 6227–6232.

11. Vaillancourt, F.H.; Barbosa, C.J.; Spiro, T.G.; Bolin, J.T.; Blades, M.W.; Turner, R.F.B.; Eltis, L.D. *J. Am. Chem. Soc.* **2002**, *124*, 2485-2496.

12. Kovaleva, E. G.; Lipscomb, J.D. *Science* **2007**, *316*, 453-457.

13. Koehntop, K.D.; Emerson, J.P.; Que, L., Jr. *J. Biol. Inorg. Chem.* **2005**, *10*, 87-93.

14. Kovaleva, E.G.; Lipscomb, J.D. *Nature Chem. Biol.* **2008**, *4*, 186-193.

15. Bruijnincx, P.C.A.; van Koten, G.; Gebbink, R.J.M.K. *Chem. Soc. Rev.* **2008**, *37*, 2716-2744.

16. Kreisberg-Zakarin, R.; Borovok, I.; Yanko, M.; Frolow, F.; Aharonowitz, Y.; Cohen, G. *Biophys. Chem.* **2000**, *86*, 109-118.

17. Costas, M.; Mehn, M.P.; Jensen, M.P.; Que, L. Jr. *Chem. Rev.* **2004**, *104*, 939-986.

18. Straganz, G.D.; Nidetsky, B. *Chembiochem* **2006**, *7*, 1536-1548.

19. Leitgeb, S.; Nidetsky, B. *Biochem. Soc. Trans.* **2008**, *36*, 1180-1186.

20. Pierce, B.S.; Gardner, J.D; Bailey, L.J.; Brunold, T.C.; Fox, B.G. *Biochemistry* **2007**, *46*, 8568-8578.

21. Joseph, C.A.; Maroney, M.J. *Chem. Commun.* **2007**, 3338-3349.

22. Straganz, G.D.; Glieder, A.; Brecker, L.; Ribbons, D.W.; Steiner, W. *Biochem. J.* **2003**, *369*, 573-581.

23. Straganz, G.D.; Hofer, H.; Steiner, W.; Nidentzky, B. *J. Am. Chem. Soc.* **2004**, *126*, 12202-12203.

24. Straganz, G.D.; Diebold, A.R.; Egger, S.; Nidentzky, B.; Solomon, E.I. *Biochemistry* **2010**, *49*, 996-1004.

25. Leitgeb, S.; Straganz, G.D.; Nidetzky B. *Biochem. J.* **2009**, *418*, 403-411.

26. Straganz, G.; Brecker, L.; Weber, H.J.; Steiner, W.; Ribbons, D.W. *Biochem. Biophys. Res. Commun.* **2002**, *297*, 232-236.

27. Chen, J.; Li, W.; Wang, M.Z.; Zhu, G.Y.; Liu, D.Q.; Sun, F.; Hao, N.; Li, X. M.; Rao, Z.H.; Zhang, X. C. *Protein. Sci*. **2008**, *17*, 1362-1373.

28. Matera, I.; Ferraroni, M.; Burger, S.; Scozzofava, A.; Stolz, A.; Briganti, F. *J. Mol. Biol.* **2008**, *380*, 856-868.

29. Hinter, J.P.; Lechner, C.; Riegert, U.; Kuhm, A.E.; Storm, T.; Reemtsma, T.; Stolz, A. *J. Bacteriol.* **2001**, *183*, 6936-6942.

30. Hinter, J.P.; Reemtsma, T.; Stolz, A. *J. Biol. Chem.* **2004**, *279*, 37250-37260.

31. Iwabuchi, T.; Harayama, S. *J. Biol. Chem.* **1998**, *273*, 8332-8336.

32. Siewert, I.; Limberg, C. *Angew. Chem. Int. Ed.* **2008**, *47*, 7953-7956.

33. Straganz, G.D,; Nidetzky, B. *J. Am. Chem. Soc.* **2005**, *127*, 12306-12314.

34. Pau, M.Y.M.; Davis, M.I.; Orville, A.M.; Lipscomb, J.D.; Solomon, E.I. *J. Am. Chem. Soc.* **2007**, *129*, 1944-1958.

35. Pau, M.Y.M.; Lipscomb, J.D.; Solomon, E.I. *Proc. Natl. Acad. Sci. U.S.A.* **2007**, *104*, 18355-18362.

36. Lipscomb, J.D. *Curr. Opin. Struct. Biol.* **2008**, *18*, 644-649.

37. Holm, R.H.; Solomon, E.I. *Chem. Rev.* **2004**, *104*, 347-348.

38. Grzyska, P.K.; Muller, T.A.; Campbell, M.G. Hausinger, R.P. *J. Inorg. Biochem.* **2007**, *101*, 797-808.

39. Han, S.; Eltis, L.D.; Timmis, K.N.; Muchmore, S.W. Bolin, J.T. *Science* **1995**, *270*, 976-980.

40. Xun, L.Y.; Bohuslavek, J.; Cai, M.A. *Biochem. Biophys. Res. Commun*. **1999**, *266*, 322-325.

41. Xu, L.; Resing, K. Lawson, S.L.; Babbitt, P.C.; Copley, S.D. *Biochemistry* **1999**, *38*, 7659-7669.

42. Nagata, Y.; Endo, R.; Ito, M.; Ohtsubo, Y.; Tsuda, M. *Appl. Microbiol. Biotechnol.* **2007**, *76*, 741-752.

43. Bruijnincx, P.C.A.; Lutz, M. Spek, A.L; Hagan, W.R.; Weckhuysen, B.M.; van Koten, G.; Gebbink, R.J.M.K. *J. Am. Chem. Soc.* **2007**, *129*, 2275-2286.

44. Kitajima, N.; Amagai, H.; Tamura, N.; Ito, M.; Morooka, Y.; Heerwegh, K.; Penicaud, A.; Mathur, R.; Reed, C.A.; Boyd, P.D.W. *Inorg. Chem*. **1993**, *32*, 3583-3584.

45. Ogihara, T.; Hikichi, S.; Akita, M. Moro-oka, Y. *Inorg. Chem.* **1998**, *37*, 2614-2615.

46. Mukherjee, A.; Cranswick, M.A.; Chakrabarti, M.; Paine, T.K.; Fujisawa, K.; Munck, E. Que, L. *Inorg. Chem.* **2010**, *49*, 3618-3628.

47. Paine, T.K.; Zheng, H.; Que, L., Jr. *Inorg. Chem.* **2005**, *44*, 474-476.

48. Mehn, M.P.; Fujisawa, K.; Hegg, E.L.; Que, L. Jr. J. Am. Chem. Soc. 2003, 125, 7828-7842.

49. Diebold, A.R.; Neidig, M.L.; Moran, G.R.; Straganz, G.D.; Solomon, E.I. *Biochemistry* **2010**, *49*, 6945-6952.

50. Reger, D.L.; Gardinier, J.R.; Elgin, J.D.; Smith, M.D.; Hautot, D.; Long, G.J.; Grandjean, F. *Inorg. Chem.* **2006**, *45*, 8862-8875.

51. Reger, D.L.; Elgin, J.D.; Smith, M.D.; Grandjean, F.; Rebbouh, L.; Long, G.J.; *Polyhedron* **2006**, *25*, 2616-2622.

52. Calogero, S.; Lobbia, G.G.; Cecchi, P.; Valle, G.; Friedl, J. *Polyhedron* **1994**, *13*, 87-97.

53. Oliver, J.D.; Mullica, D.F.; Hutchinson, B.B.; Milligan, W.O. *Inorg. Chem.* **1980**, *19*, 165-169.

54. Addison, A.W.; Rao, T.N.; Reedijk, J.; Vanrijn, J.; Verschoor, G.C. *J. Chem Soc., Dalton Tran.* **1984**, 1349-1356.

55. Kunz, P.C.; Klaui, W. *Collect. Czech. Chem. Commun.* **2007**, *72*, 492-502.

56. Sheldrick, G.M. *Acta. Crystallogr. Sect. A* **2008**, *64*, 112-122.

57. Dolomanov, O.V.; Bourhis, L.J.; Gildea, R.J.; Howard, J.A.K.; Puschmann, H. *J. Appl. Crystallogr.* **2009**, *42*, 339-341.

58. Neese, F. *ORCA - ab initio, Density Functional and Semi-empirical Program Package*, version 2.7; University of Bonn: Bonn Germany, **2009**.

59. Beck, A.D. *J. Chem. Phys.* **1986**, *84*, 4524-4529.

60. Perdew, J.P. *Phys. Rev. B* **1986**, *33*, 8822-8824.

61. Schafer, A.; Horn, H.; Ahlrichs, R. *J. Chem. Phys.* **1992**, *97*, 2571-2577.

62. Schafer, A.; Huber, C.; Ahlrichs, R. *J. Chem. Phys.* **1994**, *100*, 5829-5835.

63. Becke, A.D. *J. Chem. Phys.* **1993**, *98*, 5648-5652.

64. Becke, A.D. *J. Chem. Phys.* **1993**, *98*, 1372-1377.

65. Lee, C.T.; Yang, W.T.; Parr, R.G. *Phys. Rev. B* **1988**, *37*, 785-789.

66. Stratmann, R.E.; Scuseria, G.E.; Frisch, M.J. *J. Chem. Phys.* **1998**, *109*, 8218-8224.

67. Casida, M.E.; Jamorski, C.; Casida, K.C.; Salahub, D.R. *J. Chem. Phys.* **1998**, *108*, 4439-4449.

68. Bauernschmitt, R.; Ahlrichs, R. *Chem. Phys. Lett.* **1996**, *256*, 454-464.

69. Hirata, S.; Head-Gordon, M. *Chem. Phys. Lett.* **1999**, *314*, 291-299.

70. Hirata, S.; Head-Gordon, M. *Chem. Phys. Lett.* **1999**, *302*, 375-382.

71. Laaksonen, L. *J. Mol. Graphics* **1992**, *10*, 33-34.

72. Solomon, E.I.; Brunold, T.C..; Davis, M.I.; Kemsley, J.N.; Lee, S.K..; Lehnert, N.; Neese, F.; Skulan A.J.; Yang, Y.S.; Zhou, J. *Chem. Rev.* **2000**, *100*, 235-349.

73. Bugg, T.D.H. *Curr. Op. Chem. Biol.* **2001**, *5*, 550-555.

74. Bugg, T.D.H.; Lin, G. *Chem. Commun*. **2001**, *11*, 941-953.

75. Machonkin, T.E., Doerner, A.E. *Biochemistry* **2011**, *50*, 8899-8913.

76. Machonkin, T.E.; Holland, P.L.; Smith, K.N.; Liberman, J.S.; Dinescu, A.; Cundari, T.R., Rocks, S.S. *J. Biol. Inorg. Chem*. **2010**, *15*, 291-301.

77. Yin, Y.; Zhou, N.Y. *Curr. Microbiol*. **2010**, *61*, 471-476.

78. Xun, L.Y.; Bohuslavek, J.; Cai, M.A. *Biochem. Biophys. Res. Commun*. **1999**, *266*, 322-325.

79. Lin, G.; Reid, G.; Bugg, T.D.H.; *J. Am. Chem. Soc.* **2001**, *123*, 5030-5039.

80. Jo, D.H., Que. L. Jr.; Angew. *Chem. Int. Ed.* **2000**, *39*, 4284-4287.

81. Beck, A.; Weibert, B.; Burzlaff, N.I. *Eur. J. Inorg. Chem*. **2001**, 521-527.

82. Beck, A.; Barth, A.;Hulbner, E.; Burzlaff, N.I. *Inorg. Chem*. **2003**, 42, 7182-7188.

83. Brown, R.S.; Huguet, J. *Can. J. Chem*. **1980**, *58*, 889-901.

84. Breslow, R.; Hunt, J.T., Smiley, R.; Tarnowski, T. *J. Am. Chem. Soc.* **1983**, *105*, 5337-5342.

85. Slebocka-Tilk, H.; Cocho, J.L., Frakman, Z., Brown, R.S. *J. Am. Chem. Soc.* **1984**, *106*, 2421-2431.

86. Kimblin, C.; Allen, W.E., Parkin, G. J. *Chem. Soc., Chem. Commun***. 1995**, 1813-1815.

87. Lynch, W.E.; Kurtz, J.D.M.; Wang, S. Scott. R.A. *J. Am. Chem. Soc.* **1994**, *116*, 11030-11038.

88. Kunz, P.C.; Reib, G.J.; Frank, W.; Klaui, W. *Eur. J. Inorg. Chem.* **2003**, 3945-3951.

89. Malkhasian, A.Y.S.; Nikolovski, B.; Kucera, B.E.; Loloee, R.; Chavez, F.A. *Z. Znorg. Allg. Chem.* **2007**, *633*, 1000-1005.

90. Batten, M.P.; Canty, A.J.; Cavell, K.J.; Ruther, T.; Skelton, B.W.; White, A.H. *Acta. Crystallogr. C.* **2004**, *60*, M311-M313.

91. Wu, F.J.; Kurtz, D.M. Jr. *J. Am. Chem. Soc*. **1989**, *111*, 6563-6572.

92. Wu, F.J.; Kurtz, D.M.; Hagen, K.S.; Nymanm, P.D.; Debrunner, P.G., Vankai, V.A. *Inorg. Chem*, **1990**, *29*, 5174-5183.

93. Vankai, V.A.; Newton, M.G., Kurtz, D. Jr. *Inorg. Chem.* ***1992****, 31*, 342-343.

94. McDevitt, M.R.; Addison, A.W.; Sinn, E.; Thompson, L.K. *Inorg. Chem.* **1990**, *29*, 3425-3433.

95. Oh, N.Y.; Seo, M.S.; Lim, M.H.; Consugar, M.B.; Park, M.J.; Rohde, J.U.; Han, J.; Kim, K.M.; Kim, J. Que, L. Jr.; Nam, W. *Chem. Commun.* **2005**, 5644-5646.

96. Taktak, S.; Flook, M.; Foxman, B.M.; Que, L. Jr.; Rybak-Akimova, E.V. *Chem. Commun.* **2005**, 5301-5303.

97. Makhlynets, O.V.; Das, P.; Taktak, S.; Flook, M.; Mas-Balleste, R.; Rybak-Akimova, E.V.; Que, L. *Chem.-Eur. J.* **2009**, *15*, 13171-13180.

98. Groce, S.L; Lipscomb, J.D. *Biochemistry* **2005**, *44*, 7175-7188.

99. Edwards, P.G.; Harrison, A.; Newman, P.D.; Zhang, W.J. *Inorg. Chim. Acta.* **2006**, *359*, 3549-3556.